



The Global Magneto-ionic Medium Survey: A Faraday Depth Survey of the Northern Sky Covering 1280–1750 MHz

M. Wolleben^{1,2}, T. L. Landecker¹, K. A. Douglas^{1,3,4}, A. D. Gray¹, A. Ordog^{1,3,5}, J. M. Dickey⁶, A. S. Hill^{1,5}, E. Carretti⁷, J. C. Brown³, B. M. Gaensler⁸, J. L. Han^{9,10,11}, M. Haverkorn¹², R. Kothes¹, J. P. Leahy¹³, N. McClure-Griffiths¹⁴, D. McConnell^{14,15}, W. Reich¹⁶, A. R. Taylor^{17,18}, A. J. M. Thomson¹⁹, and J. L. West⁸

¹National Research Council Canada, Herzberg Research Centre for Astronomy and Astrophysics, Dominion Radio Astrophysical Observatory, P.O. Box 248, Penticton, BC V2A 6J9, Canada; tom.landecker.drao@gmail.com

²Skaha Remote Sensing Ltd., 3165 Juniper Drive, Naramata, BC V0H 1N0, Canada

³Department of Physics and Astronomy, University of Calgary, 2500 University Drive, Calgary, AB T2N 1N4, Canada

⁴Physics and Astronomy Department, Okanagan College, 1000 KLO Road, Kelowna, BC V1Y 4X8, Canada

⁵Department of Computer Science, Mathematics, Physics, and Statistics, University of British Columbia, Okanagan Campus, 3187 University Way, Kelowna, BC V1V 1V7, Canada

⁶School of Natural Sciences, Private Bag 37, University of Tasmania, Hobart, Tasmania 7001, Australia

⁷INAF—Istituto di Radioastronomia, via P. Gobetti 101, I-40129 Bologna, Italy

⁸Dunlap Institute for Astronomy and Astrophysics, University of Toronto, 50 St. George Street, TO M5S 3H4, Canada

⁹National Astronomical Observatories, CAS, Jia-20 DaTun Road, Chaoyang District, Beijing 100101, People's Republic of China

¹⁰School of Astronomy and Space Sciences, University of the Chinese Academy of Sciences, Beijing 100049, People's Republic of China

¹¹CAS Key Laboratory of FAST, NAOC, Chinese Academy of Sciences, Beijing 100101, People's Republic of China

¹²Radboud University Nijmegen, P.O. Box 9010, 6500 GL Nijmegen, The Netherlands

¹³Jodrell Bank Centre for Astrophysics, Department of Physics and Astronomy, The University of Manchester, Manchester M13 9PL, UK

¹⁴Research School of Astronomy and Astrophysics, Australian National University, Cotter Road, Weston Creek, ACT 2611, Australia

¹⁵CSIRO Astronomy & Space Science, P.O. Box 76, Epping, NSW 1710, Australia

¹⁶Max-Planck-Institut für Radioastronomie, D-53121 Bonn, Auf dem Hügel 69, Germany

¹⁷Department of Astronomy, University of Cape Town, Rondebosch 7701, Republic of South Africa

¹⁸Department of Physics, University of Western Cape, Republic of South Africa

¹⁹CSIRO Astronomy & Space Science, P.O. Box 1130, Bentley, WA 6102, Australia

Received 2021 January 30; revised 2021 April 9; accepted 2021 April 12; published 2021 June 29

Abstract

The Galactic interstellar medium hosts a significant magnetic field, which can be probed through the synchrotron emission produced from its interaction with relativistic electrons. Linearly polarized synchrotron emission is generated throughout the Galaxy and, at longer wavelengths, modified along nearly every path by Faraday rotation in the intervening magneto-ionic medium. Full characterization of the polarized emission requires wideband observations with many frequency channels. We have surveyed polarized radio emission from the Northern sky over the range 1280–1750 MHz, with channel width 236.8 kHz, using the John A. Galt Telescope (diameter 25.6 m) at the Dominion Radio Astrophysical Observatory, as part of the Global Magneto-Ionic Medium Survey. The survey covered 72% of the sky, decl. -30° to $+87^\circ$ at all R.A. The intensity scale was absolutely calibrated, based on the flux density and spectral index of Cygnus A. Polarization angle was calibrated using the extended polarized emission of the Fan Region. Data are presented as brightness temperatures with angular resolution $40'$. Sensitivity in Stokes Q and U is 45 mK rms in a 1.18 MHz band. We have applied rotation measure synthesis to the data to obtain a Faraday depth cube of resolution 150 rad m^{-2} and sensitivity 3 mK rms of polarized intensity. Features in Faraday depth up to a width of 110 rad m^{-2} are represented. The maximum detectable Faraday depth is $\pm 2 \times 10^4 \text{ rad m}^{-2}$. The survey data are available at the Canadian Astronomy Data Centre.

Unified Astronomy Thesaurus concepts: [Polarimetry \(1278\)](#); [Polarimeters \(1277\)](#); [Spectropolarimetry \(1973\)](#); [Radio telescopes \(1360\)](#); [Calibration \(2179\)](#); [Interstellar magnetic fields \(845\)](#); [Milky Way magnetic fields \(1057\)](#)

1. Introduction

The magnetic field of the Galaxy is a significant reservoir of energy within the interstellar medium (Ferrière 2001; Heiles & Haverkorn 2012). It supports the Galactic disk (Boulares & Cox 1990; Hill et al. 2012), it is profoundly influential in star formation (Padoan & Nordlund 2011), and it is central to particle acceleration (Urošević et al. 2019). Theories have been developed of the origin of the field in a Galactic dynamo (Beck et al. 1996; Moss & Sokoloff 2019) and of the impact of the magnetic energy reservoir in shaping galaxies (Kim et al. 1996). While its significance is well appreciated (Han 2017), the magnetic field remains a component of the interstellar medium that is difficult to observe and measure.

Of interest to us is synchrotron emission, generated throughout the Galaxy when relativistic electrons interact with Galactic magnetic fields. The magnetic field imprints its direction on the radio signal, which is linearly polarized with orientation perpendicular to the field at the point of emission. At short wavelengths, synchrotron emission carries its polarization state to our telescopes (for example, the Wilkinson Microwave Anisotropy Probe (WMAP) data at 23 GHz; Bennett et al. 2013) and yields a two-dimensional portrait of the magnetic field configuration in the Galaxy. At longer radio wavelengths, the polarization state is altered, often profoundly, by Faraday rotation occurring in magnetized ionized regions along the propagation path. Synchrotron emission is generated throughout the Galaxy, and Faraday rotation occurs everywhere; the consequent intermingling of

emission and rotation complicates interpretation of polarization observations. Faraday rotation largely obscures the original field directions; nevertheless, it can be exploited to give three-dimensional information on magnetic field configurations in the intervening medium.

Extensive surveys at single frequencies (e.g., Brouw & Spoelstra 1976; Reich et al. 2004; Wolleben et al. 2006; Sun et al. 2007; Testori et al. 2008; Gao et al. 2010; Carretti et al. 2019) and aperture-synthesis surveys in the Galactic plane (Haverkorn et al. 2006; Landecker et al. 2010) have provided two-dimensional portraits of the polarized radio sky. In combination with Faraday rotation toward point sources (Han et al. 2006; Brown et al. 2007; Taylor et al. 2009; Van Eck et al. 2021), these surveys have contributed to three-dimensional reconstructions of the magnetic field in the Galactic disk and halo (Sun et al. 2008; Van Eck et al. 2011; Jansson & Farrar 2012; Jaffe et al. 2013; Jaffe 2019). Here we take the next step, mapping Faraday depth over the entire sky to generate a data set that can further elucidate the three-dimensional structure of the Galactic magnetic field.

A source of polarized radio emission is described by the complex polarization vector at the point of emission,

$$\mathbf{P}_0 = \mathbf{Q} + i\mathbf{U} = P_0 e^{2i\chi_o}, \quad (1)$$

where \mathbf{Q} and \mathbf{U} are the Stokes parameters describing the state of linear polarization, P_0 is the polarized intensity, and χ_o is the polarization angle. If a Faraday rotating region, entirely separate from the emission region, lies along the intervening path, then, at wavelength λ , the polarization angle is rotated by

$$\Delta\chi = 0.812\lambda^2 \int n_e B_{\parallel} dl = \lambda^2 \text{RM}, \quad (2)$$

where B_{\parallel} is the line-of-sight component of the magnetic field in μG , n_e is the electron density in cm^{-3} , l is the path length in parsecs, and the integral is computed along the entire line of sight through the Faraday rotating region from the source to the observer. After Faraday rotation, the observed polarization vector is

$$\mathbf{P}(\lambda^2) = P_0 e^{2i(\chi_o + \lambda^2 \text{RM})} = P_0 e^{2i\lambda^2 \text{RM}}. \quad (3)$$

RM in Equations (2) and (3) is the rotation measure, a characteristic of the Faraday rotating region, which can be measured as

$$\text{RM} = \frac{d\chi}{d\lambda^2}. \quad (4)$$

Burn (1966) was the first to describe Faraday rotation in the more complex situation of mixed emission and rotation, and we adopt his analysis. The operation of Faraday rotation, expressed in Equation (2), is, of course, unchanged, but Burn introduced Faraday depth, ϕ , a quantity analogous to RM, defined as

$$\phi(r) = 0.812 \int_r^0 n_e B_{\parallel} dl, \quad (5)$$

where the integral is now calculated only along the line of sight from an emitting volume-element at a distance, r , from the observer, not through the entire magneto-ionic material in that direction.²⁰ Every emitting volume along the line of sight has

associated with it a value of ϕ , and the observed polarized signal, $\mathbf{P}(\lambda^2)$, at any wavelength is the integrated sum of the Faraday-rotated emission at all Faraday depths:

$$\mathbf{P}(\lambda^2) = \int_{-\infty}^{\infty} \mathbf{P}(\phi) e^{2i\lambda^2\phi} d\phi. \quad (6)$$

This has the form of a Fourier transform, and Burn (1966) defined the Faraday dispersion function $\mathbf{F}(\phi)$ as the Fourier conjugate of $\mathbf{P}(\lambda^2)$,

$$\mathbf{F}(\phi) = \int_{-\infty}^{\infty} \mathbf{P}(\lambda^2) e^{-2i\lambda^2\phi} d\lambda^2. \quad (7)$$

When Burn (1966) laid out these relationships, they could not be implemented because radio telescope technology and computing were not adequate for the collection and analysis of the required data. Four decades toppled those barriers, and Brentjens & de Bruyn (2005) developed RM synthesis on the basis of Burn's equations. The technique has since been applied extensively to data from aperture-synthesis telescopes, starting with de Bruyn & Brentjens (2005).

The Global Magneto-Ionic Medium Survey (GMIMS) has set out to provide the data for an improved understanding of the three-dimensional magnetic field of the Galaxy, by mapping polarized emission over the entire sky, both in the Northern and Southern hemispheres (Wolleben et al. 2009). The Galactic polarized emission fills the sky, with structure on all scales, and the only tools able to measure this extended structure are single-antenna radio telescopes. GMIMS is applying RM synthesis for the first time to data from such telescopes. The aim is full coverage from 300 to 1800 MHz, with many narrow frequency channels. GMIMS aspires beyond surveys of polarized emission, to produce surveys of Faraday depth. When complete, the GMIMS data set will provide a resolution in angle of the order of 1° , and, after RM synthesis, a resolution in Faraday depth of the order of 5 rad m^{-2} with a sensitivity to structures in Faraday depth space as large as 110 rad m^{-2} . For technical reasons, the frequency band has been divided into three sub-bands, 300–800, 800–1300, and 1300–1800 MHz (where the frequency boundaries are approximate). The sky naturally divides into North and South, so the entire project will comprise six *component* surveys. Observations for two component surveys in the South (300–870 and 1300–1800 MHz) have been completed with the Parkes 64 m Telescope; data for 300–480 MHz, over the decl. range $-90^\circ \leq \delta \leq 20^\circ$, have been published (Wolleben et al. 2019) and are now publicly available.²¹

Here we describe a GMIMS component survey of the Northern sky, covering 1280 to 1750 MHz, and spanning decl. $-30^\circ \leq \delta \leq +87^\circ$, observed using the John A. Galt Telescope (diameter 25.6 m) at the Dominion Radio Astrophysical Observatory (DRAO). We present the survey data, which are now being made available to the astronomical community. The data described here have already been used to study the two brightest polarized regions of the Northern sky, the North Polar Spur (Sun et al. 2015), and the Fan Region (Hill et al. 2017). A region of complex polarized emission was analyzed by Wolleben et al. (2010a). Dickey et al. (2019) applied moment techniques to the data described here, and to the GMIMS-LBS data presented by Wolleben et al. (2019).

²⁰ A magnetic field, B_{\parallel} , directed toward the observer, is, by convention, positive. For the Faraday depth, as defined in Equation (5), to be positive, r must be defined with its origin at the point of emission, not at the observer.

²¹ We denote these two surveys by the following names and abbreviations: GMIMS Low-Band South (GMIMS-LBS) and GMIMS High-Band South (GMIMS-HBS). The present survey is GMIMS High-Band North (GMIMS-HBN). No mid-band surveys have been completed yet.

Table 1
Parameters of the Polarization Survey

Antenna diameter	25.6 m
Feed	dual circular polarization
Frequency coverage (observed)	1277–1762 MHz
Frequency coverage (usable data)	1280–1750 MHz
System temperature	140 K
Angular resolution	38'.5–28'.1
Frequency resolution	485 MHz/2048 = 236.8 kHz
Coverage (decl.)	$-30^\circ < \delta < +87^\circ$ (J2000)
Coverage (R.A.)	$0^h < \text{R.A.} < 24^h$ (J2000)
Completeness of spatial sampling	95% of Full Nyquist
Observation dates	2008 April to 2012 February
Data loss to RFI ^a	~30%
Intensity calibration	absolute
Angle reference	Fan Region (see the text)

Note.

^a RFI = radio frequency interference.

In Section 2 we describe the telescope, the receiver, and the observations. Section 3 provides a detailed description of data processing. In Section 4 we examine the quality of the data from the survey by comparison with existing data. Section 5 presents the results and a selection of the data and describes a few scientific outcomes and possibilities.

2. Telescope, Receiver, and Observations

We list observational details of the survey of polarized emission in Table 1. The characteristics of the Faraday depth cube, the principal output from this work, are given in Table 5 in Section 5.

2.1. Telescope and Receiver

The receiver and polarimeter have been described in detail by Wolleben et al. (2010b), and only an outline is given here.

The Galt Telescope is a paraboloidal reflector, of diameter 25.6 m. It was equipped with a feed and receiver accepting both hands of circular polarization in a passband 1277–1762 MHz (the final bandwidth of the published data is slightly smaller in extent—see Table 1). A noise signal was coupled equally into both receiver channels with a duty cycle of 50%; its intensity was ~46 K; system temperature, including the contribution from the calibration noise signal, was ~140 K. The calibration noise source was switched at a 25 Hz rate, and the polarimeter measured all inputs relative to the calibration signal. Observations of calibration sources were made relative to the injected noise signal, as were the scan observations that make up the survey—see Section 3.2 for details of this process, which is central to the survey technique.

The polarimeter used commercial field programmable gate array (FPGA) circuit modules equipped with 8-bit analog-to-digital converters. The two inputs were digitized and processed with a fast Fourier transform routine to produce two spectra. From the left- and right-hand circular polarization inputs, L and R, four data products LL^* , RR^* , LR^* , and RL^* , were formed (* denotes the complex conjugate). The FPGA polarimeter had a maximum clock rate of 1 GHz, but the digitizer was clocked at 970 MHz to give an overall bandwidth of 485 MHz with 2048 output channels of width 236.8 kHz.

The well-known advantage of using circularly polarized receivers to measure linear polarization is that Q and U can be

measured using cross correlation (McConnell et al. 2006; Robishaw & Heiles 2018). In this implementation of polarimetry, Stokes vector $I = 0.5(LL^* + RR^*)$, and Stokes Q and U equate to LR^* and RL^* , respectively.

2.2. Observations

The observations were made between 2008 April and 2012 February. The entire survey was observed with the telescope moving up and down the meridian at 52.5 arcmin minute⁻¹. This motion, together with rotation of the Earth, produced diagonal tracks across the equatorial coordinate grid. We use the term *scan* to denote the observation along one such track, and the scan is our basic unit of data; we never deal with smaller units of data. Up and down scans slowly produced a set of interlaced observations across the sky.

Half the scans ran between decl. -30° and $+87^\circ$ with alternating scans running between -30° and $+60^\circ$ to avoid oversampling near the North Celestial Pole (NCP). The NCP itself is not accessible with this equatorially mounted telescope, imposing a Northern limit of decl. $+87^\circ$ on the survey. The southern limit, decl. -30° , was set by the latitude of the Observatory and the elevation limit of the telescope. A list of scans, the *scan library*, with predetermined starting R.A. was established. Scans were set 12' apart in R.A. to ensure full sampling (with a beamwidth of 30'–40'). A programming error led to a spacing of 24' in part of the survey, but this error did not seriously affect sampling. Scans were chosen from the library in a random sequence as part of a strategy to minimize systematic effects. Scans were made only at night to avoid effects from solar emission received in the far sidelobes, where the instrumental polarization can be as high as 50%, converting the unpolarized emission from the Sun into apparently polarized emission. Spurious polarized emission from the Sun can dominate the Milky Way polarized signal at these frequencies.

To calibrate the intensity scale of the survey, observations of one of four strong sources (Cassiopeia A, Cygnus A, Virgo A, and Taurus A) were made before and after each nighttime observation. The calibration sources are essentially point sources at the angular resolution of the telescope. Although polarized when seen at high resolution, these sources are effectively unpolarized to high accuracy when observed with our beam. Their high intensity dominated any sidelobe pickup, so these observations could be made in the daytime.

2.3. Raw Data

At the end of the observing time available for this survey in 2012 February, a total of 3536 individual sky scans had been recorded, just short of the goal of 3600 scans. The missing scans were not confined to any specific part of the sky, so, with 12' spacing between scans and a beamwidth of 30'–40', the sky coverage approached full Nyquist sampling. However, as explained below, some scans were rejected in later processing stages, which did affect the overall sky coverage to a small extent.

3. Data Reduction

Figure 1 provides a schematic diagram of the data reduction pipeline. This pipeline is described to some extent in Wolleben et al. (2010b). Here we outline in detail the steps taken to convert the raw scans into data cubes suitable for scientific

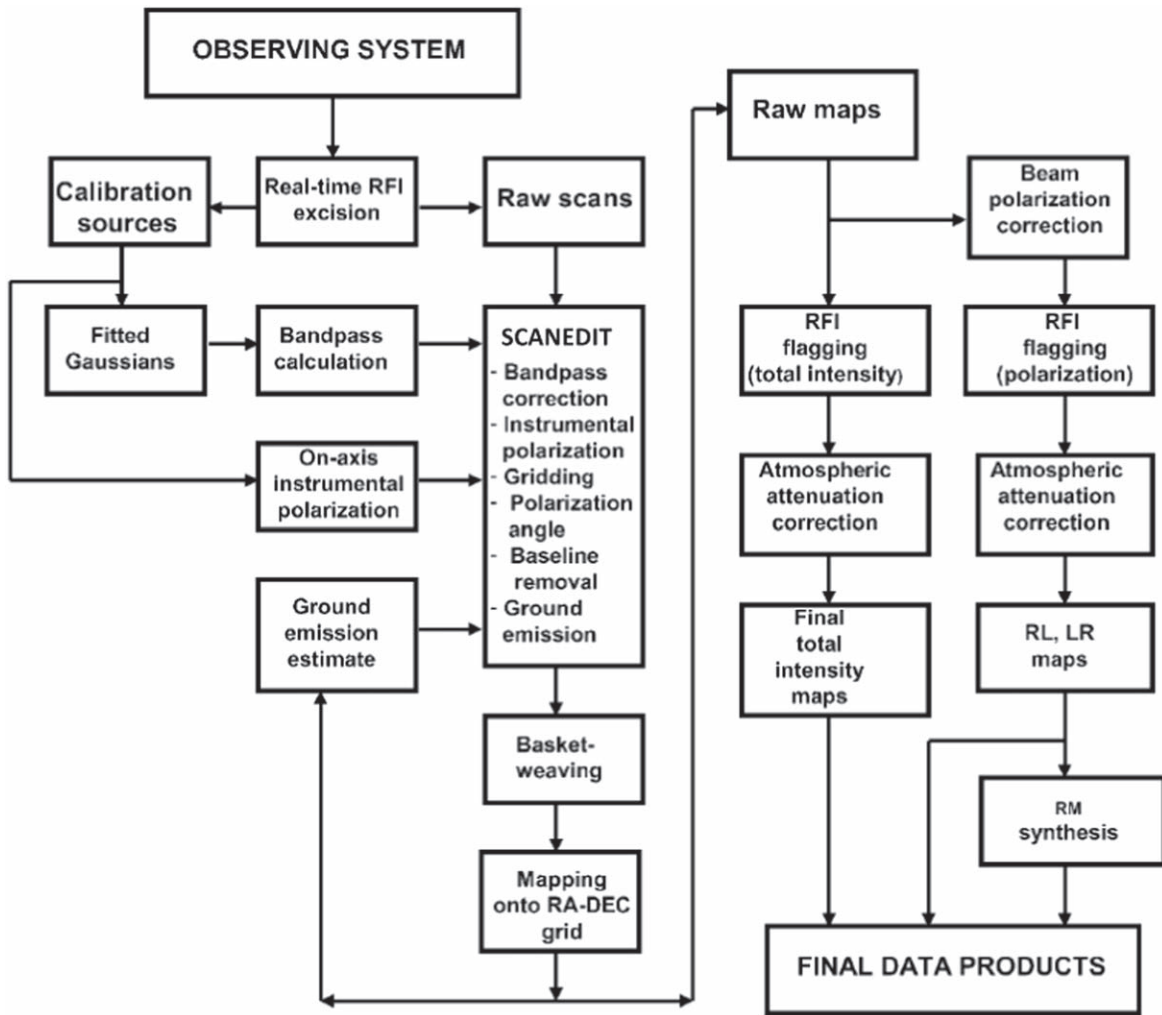


Figure 1. Schematic of the data reduction pipeline. SCANEDIT is a processing routine written for this work.

analysis. Each scan carried four correlation products, RR^* , LL^* , LR^* , and RL^* , and these data were carried through the pipeline independently.

3.1. Radio Frequency Interference

Most of the observing frequencies for our survey lie outside the bands protected for radio astronomy. The DRAO site is well protected against radio frequency interference (RFI) of terrestrial origin; it is protected physically by surrounding mountains and administratively by various levels of government. RFI from satellites is untouched by these measures, and remained a serious problem with our observations. Two stages of RFI mitigation were included in the real-time data-acquisition process: the first flagged strong, time-variable signals, and the second employed a median filter in the frequency domain that discarded data points lying outside a predetermined window around the median. Further RFI flagging was done in the final stages of the data processing pipeline (see Sections 3.10 and 3.11). Overall data loss to RFI was of the order of 30%.

3.2. Calibration

Each calibration observation consisted of a raster map of an area $2^\circ \times 2^\circ$ centered on the calibrator. A two-dimensional

Gaussian above a twisted-plane background was fitted to the observation at each frequency to provide an amplitude, and the derived amplitude was corrected for atmospheric attenuation using the equations of Gibbins (1986). Prior to calibration, the data were in units of the calibration signal. The calibration sources, with known flux densities and spectra, provided the information to convert the data units to janskys. Values of flux density, S , and spectral index, α , (where $S \propto \nu^\alpha$), were taken from the Very Large Array Low Frequency Sky Survey (VLSS) Bright Source Spectral Calculator (Helmboldt et al. 2008).²² These flux densities are on the scale established by Baars et al. (1977), but extend that work with data at lower frequencies. Table 2 gives these “literature” values, together with our adopted self-consistent values for these parameters, based on a set of observations made before our survey observations began. Both Cas A and Tau A are known to be declining in flux density, Cas A at 0.6%–0.7% per year (Reichart & Stephens 2000) and Tau A at 0.167% per year (Aller & Reynolds 1985). The value for Tau A from the VLSS Bright Source Spectral Calculator is consistent with the Baars et al. (1977) value allowing for an annual decline of 0.167% over 30 yr. The somewhat lower value from our measurements may indicate a faster decline, but that question is beyond the scope of this paper.

²² <https://lda10g.alliance.unm.edu/calspec/calspec.html>

Table 2
Primary and Secondary Gain Calibrators

Name	Literature Value		Adopted Value		Notes
	Flux Density (Jy) at 1.4 GHz	Spectral Index α	Flux Density (Jy) at 1.4 GHz	Spectral Index α	
Cyg A	1579	-1.02	1589	-1.07	1, 3
Tau A	908	-0.29	848	-0.27	1, 3
Vir A	208	-0.83	207	-0.90	1, 3
Cas A	2442	-0.78	1861	-0.77	2, 4

Note. 1—primary calibrator, 2—secondary calibrator, 3—flux density and spectral index taken from VLSS Bright Source Spectral Calibrator (Helmboldt et al. 2008), 4—flux density of Cas A decreases with time, literature flux density is for 1980, adopted flux density for epoch 2008–2012.

The calibrations provided corrections for the instrumental bandpass, and allowed correction of the small gain difference between the LL* and RR* channels. The bandpass was very stable throughout the course of the survey, and there was no significant variation of the results obtained from different calibrators.

Each night’s observations were preceded by an observation of one of the four calibration sources, and followed by a similar observation of another. All data were recorded in units of the injected noise signal, which was running continuously, but, after applying the calibration, the scans were in units of janskys, and the intensity of the injected noise signal became irrelevant. We did not rely on long-term stability of the noise diode; all that was required of it was that it be stable over the course of one night’s observations with their attached calibrations. In fact the noise diode output did vary slowly over the three years of the survey (by +13% and -6%), but this variation was so slow that it did not contribute significant error.

Since the calibration sources were unpolarized (see Section 2.2), the calibrations could also be used to correct for on-axis polarization leakage. This instrumental effect arose from signal leakage between L and R, occurring in the feed and attached waveguide devices, which are extremely stable metal structures. No changes in this leakage were expected, or detected over the 3.8 yr period of observations. (Note that this step corrected for “leakage” between the R and L channels in the feed and polarization transducer, but did not correct for instrumental polarization across the telescope beam. Correction for the latter effect was made later—see Section 3.8.) While there might have been some spurious polarized signal from the Sun in the sidelobes during the daytime calibration observations, the calibration sources are very strong, and their emission dominated sidelobe effects; the baseline removal incorporated into the fitting routine further diminished any sidelobe contributions.

Polarization angle was calibrated with observations of 3C 286 and 3C 270 in 2007 October (see Figure 6 of Wolleben et al. 2010b). Further observations of 3C 286 in 2012 November revealed no significant change. However, this calibration was later revised using a new calibration technique we developed that has more general application (for a full explanation see Section 4.3).

3.3. Processing Individual Scans

We developed an interactive tool, SCANEDIT, for processing individual scans. Every one of some 3500 scans was

inspected for data quality as the data came off the telescope. This program was the principal tool for detecting receiver and polarimeter malfunction. At this stage, some scans were discarded and observed again. In the later data processing phase, bandpass and instrumental polarization corrections, derived from the calibration observations, were applied. A ground emission and atmospheric emission profile deduced from preliminary maps was also subtracted (see Section 3.6).

3.4. Basketweaving

The individually calibrated scans were combined to produce all-sky RR*/LL*/LR*/RL* data cubes. A key step in that process was “basketweaving,” where all scans were interleaved, and crossing points between individual scans used to find offset values for each scan, so that small systematic variations between scans could be minimized. This was an iterative process, applied to the entire survey region on a channel-by-channel basis. Of the data processing steps, basketweaving placed the heaviest demands on computing resources.²³

Data products RR*, LL*, RL*, and LR* were processed separately by the basketweaving algorithm, closely following the procedure of Haslam et al. (1974). The algorithm compared the signal levels along each scan with the signal levels of all other scans that crossed this scan. Each scan will have some variations in the baseline that are systematic on timescales of minutes or hours, but these variations become random on timescales of weeks or months. When the baseline of a single scan was compared to the baselines of hundreds of other scans, it could be assumed that the baseline variations of all of the other scans averaged to zero.

For each scan, the differences between data points along this scan and all of the overlapping data points from the crossed scans were calculated. Data points had to be within 48’ of each other to be considered overlapping. There were usually data points approximately every 12’ in decl. along a scan, but, to remove noise and deal with outliers, these differences were binned with a bin width of 5° in decl. for six iterations, then 2°5 for a further four iterations. We used spline interpolation between bins. When calculating the differences, the basketweaving algorithm discarded the lowest and highest 1% of all differences for each overlap region. This effectively prevented RFI from affecting baselines.

²³ Basketweaving used the supercomputing resources provided by *WestGrid*, which is one node of *Compute Canada’s* High Performance Computing facilities, and by the Centre for High Performance Computing in Cape Town, South Africa.

At the end of the basketweaving process, the determined offsets were subtracted from each scan. The offsets in LR^* and RL^* were determined over very large areas of sky, of the order of 10^4 square degrees. We can expect Q and U to average to zero over such large areas, so no sky signal was lost. That statement is acceptably correct in our frequency range. However, at higher frequencies where Faraday rotation is negligible, it may no longer be true. For example, the 23 GHz data of Bennett et al. (2013) show polarization angle changing slowly and smoothly with sky position.

For total-intensity data (RR^* and LL^*), offset removal as the last stage of basketweaving had a more serious effect: the sky minimum at each frequency was subtracted. The incorrect zero level means that the total-intensity data cannot be used directly for computing fractional polarization or spectral indices.

3.5. Gridding

Maps were made from the data after basketweaving in order to assess data quality. Scan values falling within a square of size $12'$ on an equatorial grid were averaged, and linear interpolation filled missing values. The products at this stage of the pipeline were considered *Raw Maps*, and this point is so marked in Figure 1. The product from this stage was a set of data cubes of RR^* , LL^* , RL^* , and LR^* .

3.6. Ground Radiation

In the polarization channels LR^* and RL^* , the signal received by the telescope was a vector combination of polarized signal from the sky, instrumental polarization, and polarized ground emission. Instrumental polarization was removed by the basketweaving process, but ground emission remained in the data. Radiation from the ground entered the feed through the spillover sidelobes, which usually have strong spurious polarization, and ground radiation reached the receiver as a signal that appeared to be strongly polarized. It was therefore essential to remove the effects of ground radiation from all four polarimeter data products, not just from the total-intensity data. At the zenith, the ground contribution to total intensity was about 5 K. The polarized intensity of the ground contribution was low at the zenith, but rose with increasing zenith angle, reaching a level of ~ 0.3 K at 1.4 GHz. This is about half the polarized intensity of the brightest polarized features in the sky, and it obviously had to be removed. Ground radiation did not vary with time.

We proceeded on the assumption that, across a large area of sky, the sky polarization angle will take on a wide range of values, and Q and U will average to nearly zero. We used the R.A. range 8.5^h to 12^h , where we know that the polarized emission is low (Wolleben et al. 2006), and we averaged in R.A. The result defined the ground emission correction as a function of decl. and frequency. This correction was determined channel by channel, without any smoothing in frequency, and applied in the same way. Removal of ground radiation was an iterative process: as maps produced from the data pipeline gradually improved, the ground emission profile improved in accuracy.

In total-intensity channels, LL^* and RR^* , we used the same range of R.A. At each decl., we identified the lowest value of total intensity, and plotted these minima against decl. Given the presence of small emission features, this was not a smooth curve. We took the lower envelope of this curve as the best

estimate of the ground contribution as a function of decl., but we acknowledge that a small amount of Galactic signal may have remained in this estimate. The total-intensity profiles also include atmospheric emission (~ 2 K at the zenith at the frequencies in our band, varying as the secant of zenith angle).

3.7. Identifying and Eliminating Bad Data

Inspection of gridded images after the basketweaving process revealed some bad data. The problem was ultimately traced to a faulty cable causing variation of the calibration signal in the L receiver channel. The resulting gain jumps, of duration tens of minutes, generated prominent features in the gridded maps that no number of basketweaving iterations could remove. These artifacts were, of course, most prominent in the LL^* maps but strongly affected LR^* and RL^* maps as well. The problem was easily solved for total-intensity data: RR^* data values were unaffected, and affected LL^* data values were simply replaced by RR^* data values at the same point in the sky. This affected the final noise level to some extent, but was otherwise not a serious degradation.

This solution was obviously unsuited to polarization data, and three different approaches were considered for repairing LR^* and RL^* data, (a) keep all 3536 scans, (b) reject all scans where this problem in the L-polarization adversely affected the data quality, and (c) attempt to “fix” the problem scans by interpolating data from nearby good scans. Option (a) was rejected because of image quality. Option (b) was rejected because of data loss. This left option (c).

The spectrum of data quality in affected L scans was, of course, a continuum, and judgment had to be applied. A strategy was devised whereby acceptable L data within $30'$ of affected data were used, with appropriate distance weightings, to generate interpolated RL^* and LR^* values. If an insufficient number of good-quality neighboring data values was found (if the sum of the weights was below a threshold value) then that scan could not be “repaired.” Applying this interpolation scheme once, we recovered 1287 of the 1590 scans we had previously rejected. In a second step, we considered the “repaired” scans as good scans, and recovered another 112 scans. We did not take this interpolation process to a third step because we would then have been taking data from beyond the $30'$ circle. In this way we passed a total number of 3345 scans into the basketweaving process, giving us about 95% Nyquist sampling of the sky. Missing data points are distributed randomly across the sky.

3.8. Correction for Instrumental Polarization Across the Telescope Beam

After on-axis instrumental polarization had been corrected (Section 3.2), there remained instrumental polarization across the telescope beam, arising from feed properties, reflector properties, and aperture blockage (Ng et al. 2005; Du et al. 2016). Instrumental polarization manifests itself as leakage of Stokes I into Q and U . In a given direction, if the ratio of the telescope response to Q and I , $Q_{\text{tel}}/I_{\text{tel}}$, is nonzero, a spurious polarized signal will appear in the Q channel, and, equivalently, a nonzero ratio $U_{\text{tel}}/I_{\text{tel}}$ will have the same effect in U . Such spurious polarized signals will result whenever there is strong total-power emission that fills the beam (but not when point sources are observed). For an antenna with perfectly symmetrical structure, the off-axis polarization is symmetrical; $Q_{\text{tel}}/I_{\text{tel}}$

and $U_{\text{tel}}/I_{\text{tel}}$ take nonzero values, but average to zero across the main beam. However, the Galt Telescope has three feed-support struts, which have a strong impact on polarized radiation characteristics (Du et al. 2016), and the instrumental polarization averages to small, but still significant, values. The effects could be seen in our data along the Galactic plane, a strong extended source of emission: the central parts of the Galaxy appeared to be strongly polarized. Typical values of spurious polarized intensity in that region were 3% of the total-power signal.

We used the Galactic center region, $\ell \leq 30^\circ$, $|b| \leq 8^\circ$, to evaluate this instrumental effect. We modified the observed values of Q and U , Q_{obs} and U_{obs} , to yield Q_{mod} and U_{mod} , where

$$Q_{\text{mod}} = Q_{\text{obs}} + g I \quad (8)$$

and

$$U_{\text{mod}} = U_{\text{obs}} + h I. \quad (9)$$

Factors g and h represent the instrumental polarization. They are small numbers that can be positive or negative, and they vary with frequency. At a given frequency, g and h are constant, while the Stokes parameters vary with sky position. g and h were modified iteratively until the apparent polarized intensity in the test region was minimized. Factors g and h were then used to modify observed Q and U across the entire survey region. The effects were minimal, except in areas of very bright total intensity. In such areas, spurious polarization was suppressed by about a factor of 10.

This procedure addressed instrumental polarization across the main beam, but did nothing for sidelobe effects. Instrumental polarization produces a characteristic butterfly pattern in the Q and U sidelobes. This can be seen around very strong point sources, but it has a negligible effect on the low-level extended emission. We made no corrections for sidelobe effects.

3.9. Absolute Calibration

The survey is absolutely calibrated, and the results are presented as main-beam brightness temperatures in kelvin. The aperture efficiency of the telescope, and equivalently the gain, was measured using Cygnus A, assuming the flux density and spectrum given in Table 2. The measurement was made in 2015 October, after the completion of survey observations. Details of the measurement are given in a separate paper (Du et al. 2016), and only an outline is given here.

The temperature standards used in the calibration observation were (a) a box of absorbing foam at ambient temperature that was placed in front of and around the feed horn, and (b) the sky temperature with the telescope pointed at the zenith. The accuracy of such a measurement is critically dependent on the cold temperature; the knowledge gained in the antenna study (Du et al. 2016) was applied to estimate contributions from ground radiation and other inputs. The result was corroborated by a number of separate measurements. First, the antenna temperature generated by the noise calibration signal was measured relative to noise signals from resistors at known temperatures, one immersed in liquid Nitrogen, one at ambient temperature, and one at $\sim 100^\circ\text{C}$. Second, losses in the feed horn, the quarter-wave plate, and other waveguide components

were measured using a network analyzer. These losses amounted to about 0.3 dB, a power loss of $\sim 6\%$.

With the aperture efficiency established, the survey data could be converted into antenna temperatures, T_A , in kelvin

$$T_A = \frac{S\lambda^2}{2k\Omega} = \frac{S\eta_A A_p}{2k}, \quad (10)$$

where Ω is the total solid angle of the antenna in steradians, including sidelobes, S is the flux density in janskys, η_A is the aperture efficiency, A_p is the physical area of the telescope aperture, and k is Boltzmann’s constant. However, the quantity of astrophysical interest is the main-beam brightness temperature, T_B

$$T_B = \frac{\Omega}{\Omega_B} T_A, \quad (11)$$

where Ω_B is the solid angle contained in the main beam, and it is understood that all of the quantities are functions of frequency, ν . The beam efficiency is

$$\eta_B = \frac{\Omega_B}{\Omega}. \quad (12)$$

The difficulty in applying these equations lies in defining the limits of the main beam in the calculation of Ω_B . Some surveys are reported in units of full-beam brightness temperature, where the limits of the full beam are taken at a carefully chosen radial distance from the axis of the main beam (this limit is set at $3^\circ.5$ in the work of Reich 1982 and Reich & Reich 1986—the well-known Stockert survey at 1420 MHz). An alternative definition is to consider that the first null defines the limits of the main beam. These choices are workable for surveys at a single frequency, but are difficult to adapt to a wideband survey like that described here. We could think of no sensible way of defining a “full beam” as a function of frequency. We tried using the first null as the limit, but that moves around quite rapidly as the frequency varies, and adopting that definition would have added frequency structure to the results that could not possibly come from the Galactic radio emission. Instead we defined the “main beam” solid angle as the solid angle of a Gaussian whose half-width equals the measured half-power beamwidth, $\theta(\nu)$, of the telescope²⁴ at frequency ν . Then

$$\Omega_B = 1.13 \theta(\nu)^2. \quad (13)$$

Subsequent operations on the survey data assumed that the data had been taken with a Gaussian beam. In particular, prior to the RM synthesis operation (Section 3.11), the data were brought to a common angular resolution, the beamwidth at the lowest frequency, which was accomplished by convolution with a Gaussian of appropriate FWHM.

Figure 2 shows aperture and beam efficiencies, η_A and η_B , across the frequency band. Calculated values of η_A are shown, from Du et al. (2016). For application to processing our survey data, we fitted second-order polynomials to these data points, as shown. In Section 4.2 we discuss frequencies around 1500 MHz where we see the largest deviations of calculated values from the global fit; there we present evidence that

²⁴ Baars (2007) states that a Gaussian function is a good approximation to the beam from a tapered circular aperture down to a level of about -20 db (1%).

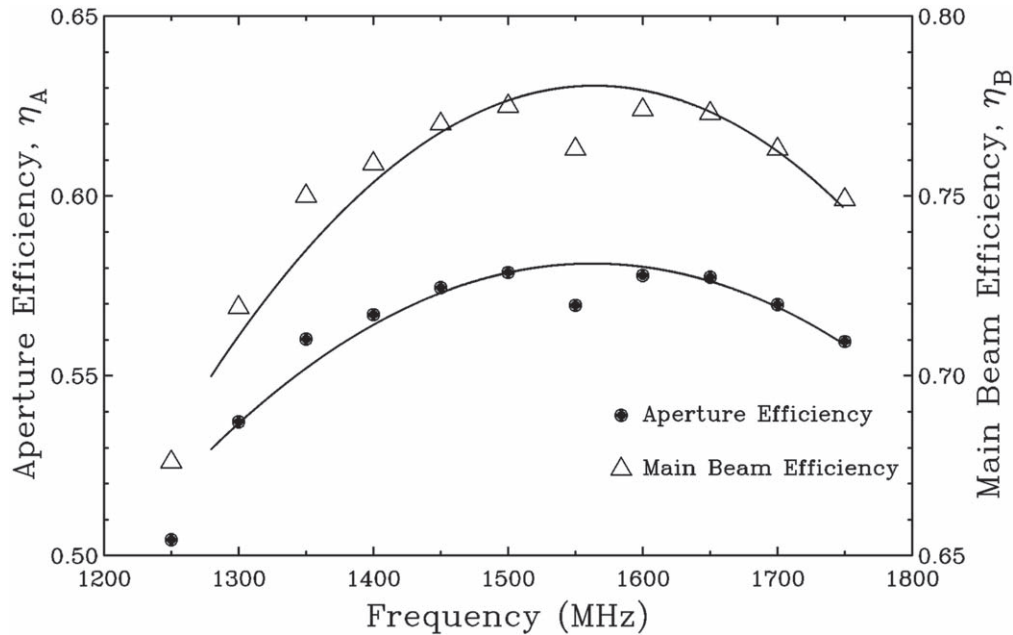


Figure 2. Aperture and beam efficiencies, η_A and η_B , as a function of frequency. Symbols show calculated values, and the curves, fitted to the calculated values, show the adopted function. For details, see the text and Du et al. (2016). Values at 1550 MHz, lower than the fitted curve, are addressed in Section 4.2.

aperture efficiency near 1550 MHz is, in fact, lower than the fitted curve, as the calculated values indicate.

3.10. Final Steps

After completion of the basketweaving process, it was clear that a few problems remained. First, there were several obvious artifacts that were related to decl. in the total-intensity maps. Second, there were distinct traces of residual RFI in the images.

The decl.-related artifacts in the total-intensity maps were more-or-less frequency independent. There was a stripe about 10° wide near decl. $+60^\circ$, and a slope in level from decl. -20° to the lower limit of the survey at -30° . We assumed that these artifacts arose from an imperfect removal of ground radiation, and we repaired them by modifying the ground radiation function.

The RFI remaining in the data appeared as amplitude changes along the scan directions. In both total-intensity and polarization data, the RFI was dealt with in the frequency domain, but the two types of data required different responses. In total-intensity images, the excursion from apparently good data values was always positive, while in polarization data, the excursion could be positive or negative. In polarization data, values exceeding five standard deviations among data points across the frequency band were replaced by no-data values. In the total-intensity data set, such simple flagging removed RFI but also flagged a large number of data points where the emission had high intensity. To eliminate this problem, a polynomial was fitted to the spectrum at each point and subtracted from the data, effectively removing the strong emission. Remaining high data values were flagged, and the removed polynomial was restored. In fitting the polynomials to the data, we ignored frequencies where RFI is always high (for example in the GPS and other satellite bands).

As a final step, the measured amplitudes of total-intensity and polarization data were corrected for atmospheric attenuation using equations from Gibbins (1986).

No correction was made for Faraday rotation in the ionosphere. The observations were made at night during solar minimum. At these times, the ionospheric RM at DRAO is usually in the range $0.5\text{--}1\text{ rad m}^{-2}$, producing a rotation of only $1^\circ\text{--}3.2^\circ$ at 1280 MHz, and correspondingly less at higher frequencies.

3.11. Rotation Measure Synthesis

To calculate Faraday depth (FD, ϕ) spectra, we used the three-dimensional RM synthesis routines in Purcell et al. (2020), based on the equations in Brentjens & de Bruyn (2005), upgraded and maintained by the Canadian Initiative for Radio Astronomy Data Analysis (CIRADA).²⁵ The code has the capability to handle pixels flagged for RFI or lacking data, and computes a rotation measure spread function (RMSF) unique to each pixel in the data cube that can then be used in the RM CLEAN deconvolution procedure (Heald 2009). We started with data cubes consisting of Stokes Q and U channel-averaged maps, covering 1276.70–1759.81 MHz, smoothed to a common angular resolution of $40'$. We averaged five adjacent channels of the original data cube to obtain 409 channels, evenly spaced in frequency by 1.18 MHz. Of the 409 channels, 132 were contaminated by RFI, including a broad frequency range spanning 1520–1640 MHz, and these were not used in the RM synthesis. For the remaining 277 channels, we used equal weighting for all frequencies.

For the frequency coverage of the survey, the resolution in Faraday depth is approximately 150 rad m^{-2} . This is slightly larger in regions with missing data in the high- and low-frequency channels, with a maximum value of 160 rad m^{-2} . The RM synthesis parameters are summarized in Table 5 (in Section 5), and an example of the RMSF is shown in Figure 3. The highest frequency used determines a maximum observable width of a broadened structure to be $\sim 110\text{ rad m}^{-2}$, which is smaller than the

²⁵ RM synthesis and RM CLEAN code on the CIRADA github: <https://github.com/CIRADA-Tools/RM>.

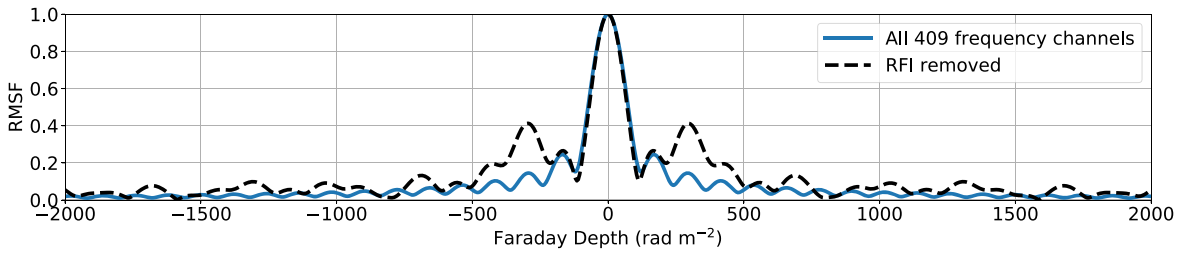


Figure 3. A representative RMSF, before removal of RFI-affected channels from the data, and after removal of those channels.

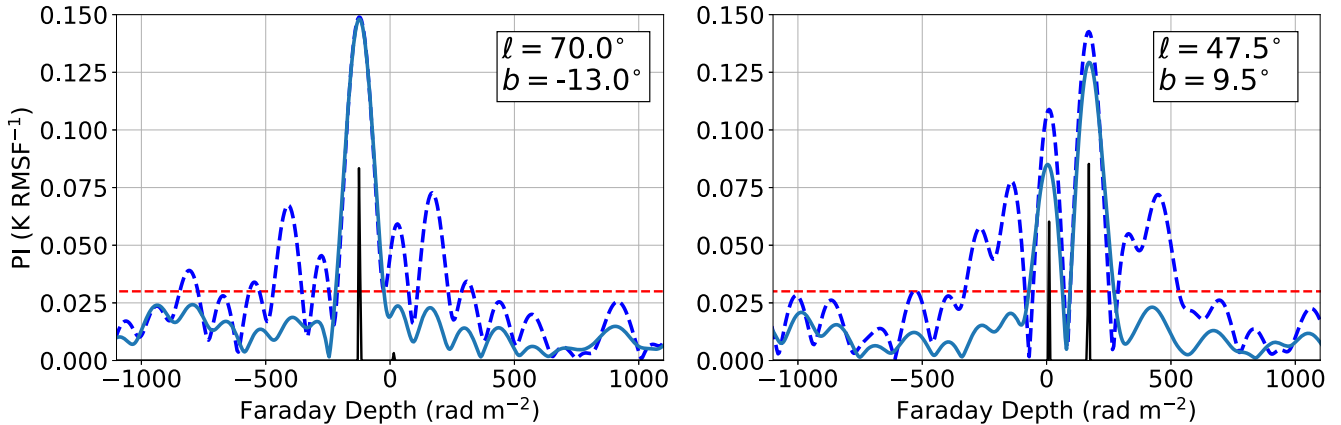


Figure 4. Two Faraday spectra. In each plot the red dotted line indicates the CLEAN limit, 0.03 K RMSF^{-1} . The dashed blue line shows the dirty spectrum, and the solid blue line shows the clean spectrum. The black lines represent the CLEAN components.

width of the RMSF. The increments in λ^2 across the full frequency range are between $4.0 \times 10^{-5} \text{ m}^2$ (high frequencies) and $1.0 \times 10^{-4} \text{ m}^2$ (low frequencies), corresponding to a maximum detectable Faraday depth between $\sim 1.9 \times 10^4 \text{ rad m}^{-2}$ (low frequencies) and $\sim 4.7 \times 10^4 \text{ rad m}^{-2}$ (high frequencies).

Faraday depth spectra were calculated over the range $-2500 \leq \phi \leq 2500 \text{ rad m}^{-2}$ in increments of 5 rad m^{-2} . This range of ϕ is well within the maximum range determined by the survey parameters, and the step size corresponds to approximately 30 samples across the FWHM of the RMSF, allowing for smoothly displayed spectra in which features such as multiple peaks are easily discernible. Figure 4 shows examples of dirty and clean spectra, together with clean components, extending over $-1000 \leq \phi \leq 1000 \text{ rad m}^{-2}$.

A universal RM CLEAN threshold was determined for the entire data set by taking the average of the polarized intensity in the spectra beyond $\pm 500 \text{ rad m}^{-2}$, which approximates the noise level. Taking a minimum of 5σ for detecting a true feature yields a CLEAN threshold of 0.03 K RMSF^{-1} . Using an iteration increment of 10%, the dirty spectra were deconvolved with the RMSF provided by the RM synthesis procedure, down to this threshold. Many of the initial “dirty” spectra have significant sidelobes around the main peak(s) that do not correspond to true features. After applying RM CLEAN, the sidelobes are reduced to below the threshold level. Over most of the sky, there is only one peak in ϕ , but a small fraction of spectra show multiple peaks or broadened structures (such as in the right-hand plot of Figure 4). Faraday cube characteristics are listed in Table 5 in Section 5. Samples from the cube, chosen to illustrate the diversity of spectra, are shown in Figure 5.

We inspected all spectra in the CLEANed Faraday depth cube within $\pm 1000 \text{ rad m}^{-2}$. Features were found in some spectra at approximately $+800 \text{ rad m}^{-2}$, and a smaller number

at -800 rad m^{-2} . Figure 6 shows the location of all Faraday depth features beyond $\pm 500 \text{ rad m}^{-2}$. Those at -800 rad m^{-2} occur at points of high total intensity. We consider all of these features to be spurious on the basis of their apparent distribution on the sky and their narrow distribution in Faraday depth. Features at $\pm 800 \text{ rad m}^{-2}$, confined to decl. below -10° (see Figure 6), are unlikely to be related to the Galaxy. These spurious features correspond to a modulation of Q and U with a period of about 80 MHz. We believe that they are byproducts of the process of determining ground radiation because they are mostly absent between R.A. 8^{h} and $12^{\text{h}} 30^{\text{m}}$ where ground radiation was evaluated (see Section 3.6). Following this investigation, we decided to publish data only over the range $-500 \leq \phi \leq 500 \text{ rad m}^{-2}$.

A small modulation with a period of $\sim 19 \text{ MHz}$ is evident in the Q and U images. This arises from interaction of the feed with the reflector (see Du et al. 2016 for some details). The modulation is less than a few percent where emission is strong, but becomes fractionally more significant at low amplitudes. The Faraday depth corresponding to this period is over 3000 rad m^{-2} , beyond the limit of our calculations.

4. Tests of Data Quality

In this section we compare our survey data to existing data, where available, and we describe some tests of internal consistency. We also estimate error in the data set.

4.1. The Amplitude Scale Near 1400 MHz

We wanted to compare our data against existing data, but that comparison had to be confined to the vicinity of 1.4 GHz, the only frequency within the range of our survey where other data sets exist. We used the T-T plot method (Costain 1960), in which the intensity from one data set was plotted against the

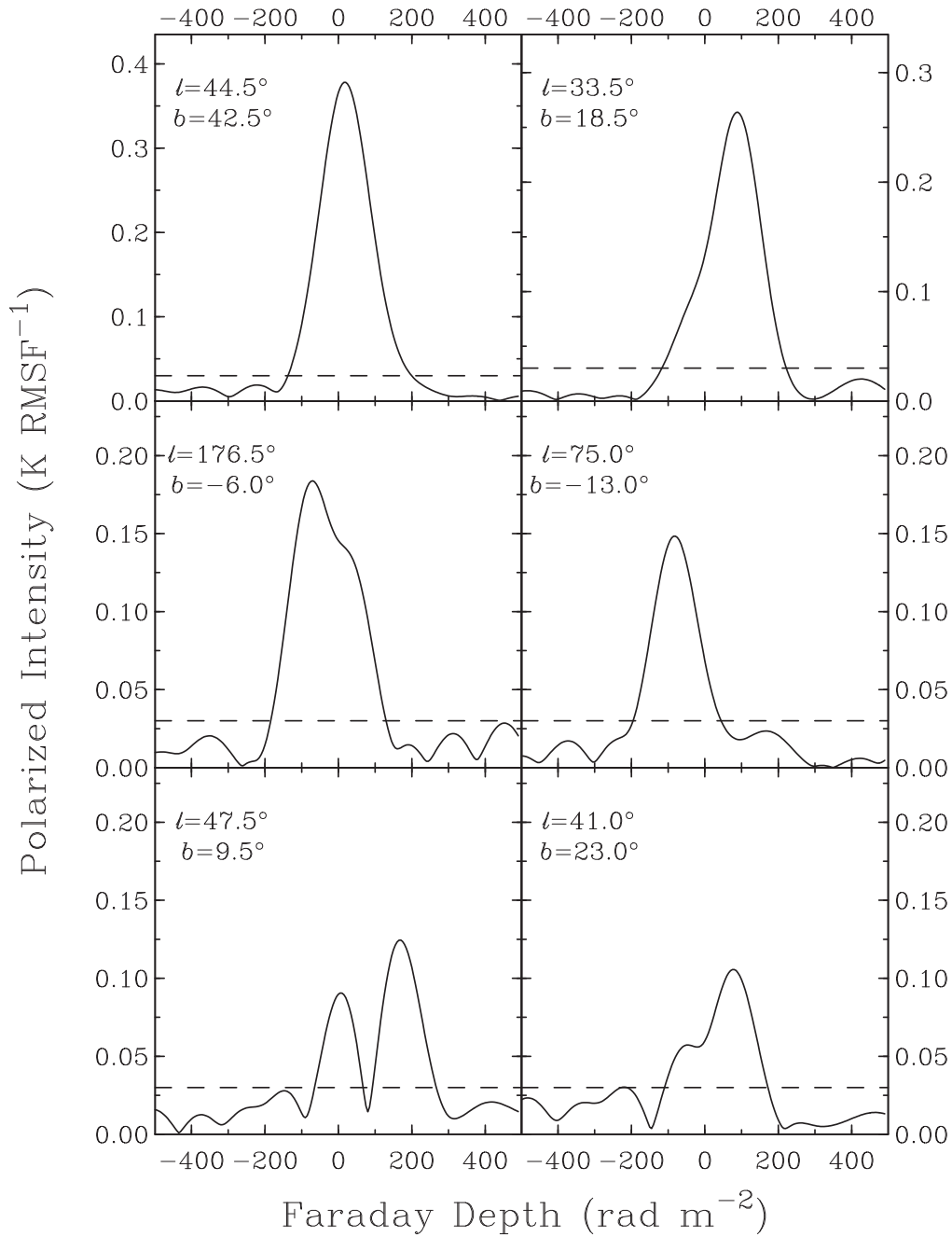


Figure 5. Faraday depth spectra after application of RM CLEAN. Sky position in Galactic coordinates is shown for each spectrum. In each plot the dashed line indicates the RM CLEAN limit, 0.03 K RMSF^{-1} . Different intensity scales are used for some spectra.

intensity from another data set at the same sky position. We made T-T plots for total intensity, I , and for polarized intensity. When the two data sets are at the same frequency, the slope of the line fitted to the points gives the average ratio between the two temperature scales.

First, we compared our I data with the Stockert data set (Reich 1982; Reich & Reich 1986) at 1420 MHz (with frequency channels chosen to match the Stockert bandpass). The comparison, over the entire range of our survey, is shown in Figure 7. The fitted line shown in the figure has a slope of 1.38. If the Stockert full-beam brightness temperatures are converted to main-beam brightness temperatures using the full-beam and main-beam solid angles given by Reich & Reich (1988), the GMIMS/Stockert ratio is 0.97. We note that the two surveys were made 30

yr apart, were independently calibrated, and used different definitions of the main beam in calculating beam solid angle. We have not made any adjustments to our intensity scale. The offset of the fitted line, about -1 K , arises from the basketweaving process, which has removed the sky minimum from our I data. We did not attempt to correct the zero level of our I data.

The main theme of our work is a study of the polarized sky, so very relevant comparisons center on the polarized emission. We made use of the data of Brouw & Spoelstra (1976), a set of carefully calibrated surveys at 408, 465, 610, 820, and 1411 MHz, made with the Dwingeloo 25 m Telescope (we refer to these five data sets collectively and separately as the *Dwingeloo data*). We compared our values of polarized intensity at 1411 MHz with the 1411 MHz Dwingeloo data;

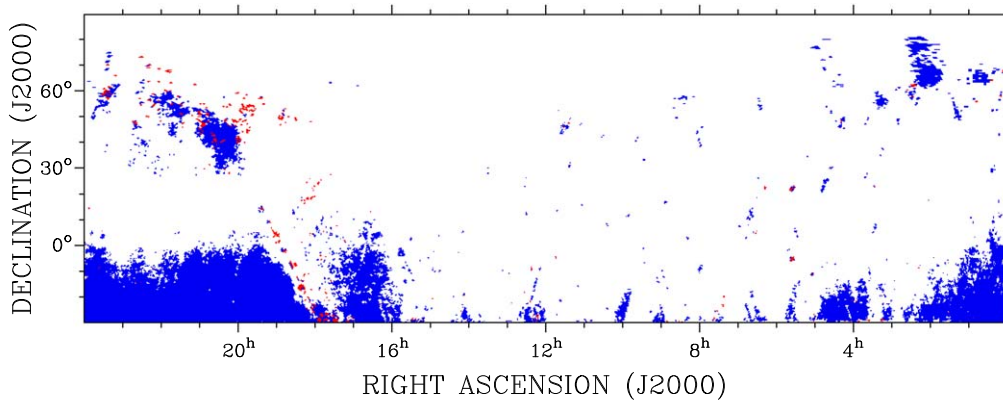


Figure 6. Locations of Faraday depth features with $|\phi| > \pm 500 \text{ rad m}^{-2}$. Blue indicates features with positive ϕ , the majority, and red indicates features with negative ϕ , only 1.5% of the total. All are considered spurious.

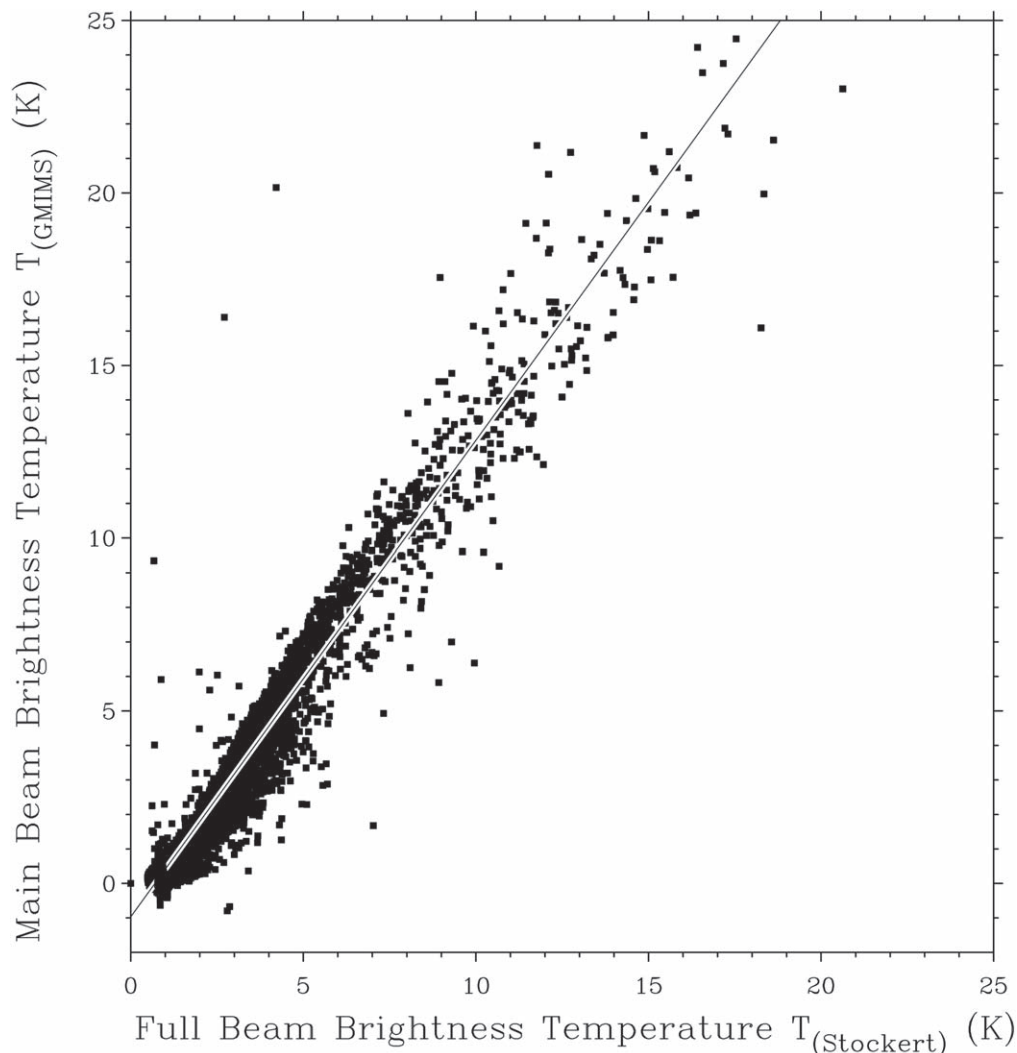


Figure 7. Main-beam brightness temperature at 1420 MHz plotted point by point against full-beam brightness temperature from the Stockert surveys (Reich 1982; Reich & Reich 1986) over the entire range of our survey. A few points at very high intensity, corresponding to small-diameter sources, are omitted. The fitted line has a slope of 1.38 and an offset of -0.97 K .

the angular resolution is almost identical to ours. Our source of Dwingeloo data was a computer-readable file giving values of polarized intensity and polarization angle over most of the sky above decl. 0° . Figure 8 shows T-T plots of polarized intensity over the two most highly polarized regions of the Northern sky,

the Fan Region and the North Polar Spur. The two scales are clearly quite similar, but there is scatter in both plots and there are outliers. To quantify the comparison, we have computed histograms of the ratio between the two surveys; these are shown in Figure 9. The histograms peak at a ratio of about 0.9,

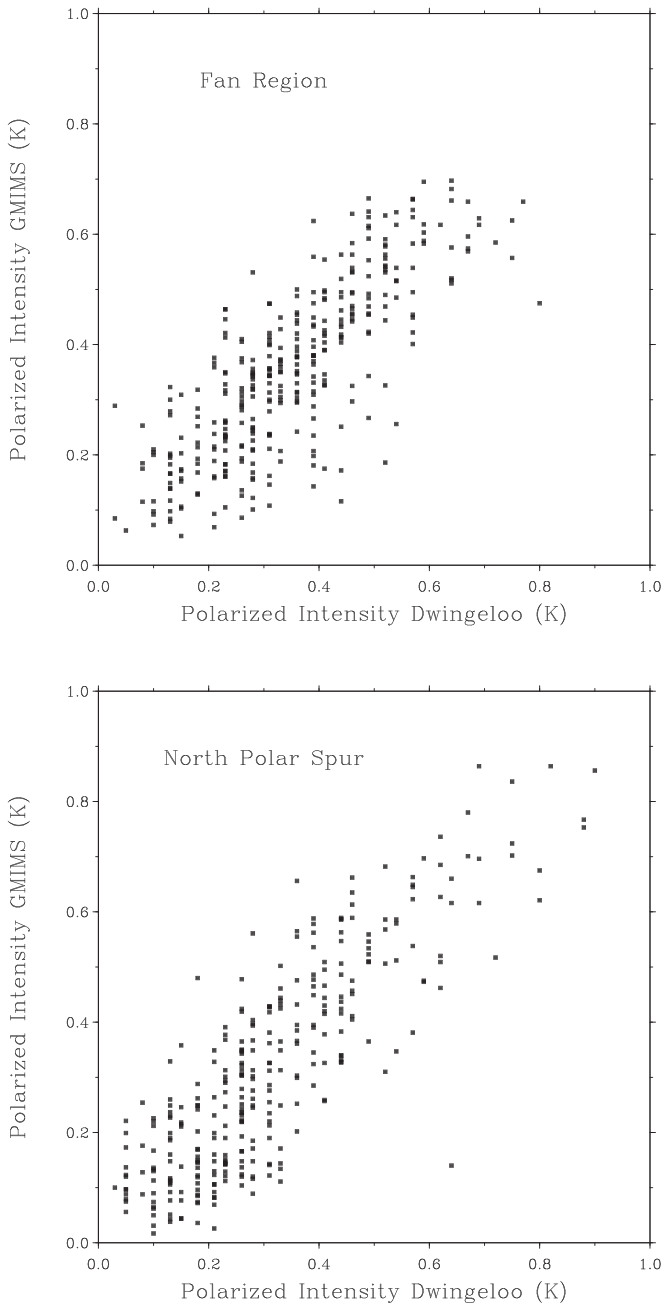


Figure 8. Polarized intensities at 1411 MHz plotted point by point against the corresponding values from the Dwingeloo survey (Brouw & Spoelstra 1976), for the Fan Region (top) and the North Polar Spur (bottom). The Fan Region data, comprising 350 sky positions, cover $110^\circ \leq \ell \leq 180^\circ$, $0^\circ \leq b \leq 30^\circ$. Data for the North Polar Spur, 319 points, cover $-30^\circ \leq \ell \leq 60^\circ$, $20^\circ \leq b \leq 80^\circ$.

implying that our polarized intensities are slightly higher than the Dwingeloo values. The two surveys have different sensitivity: Brouw & Spoelstra (1976) quote 60 mK as the mean error of their 1411 polarized intensities, while the noise on our data over the equivalent band at 1411 MHz is 25 mK. Part of the difference between the two survey scales can be attributed to slightly different definitions of the main beam, something we cannot make adjustments for.

4.2. The Amplitude Scale Across 1280–1750 MHz

We investigated the relative accuracy of the intensity scale of the survey using the total-intensity data. We generated I maps

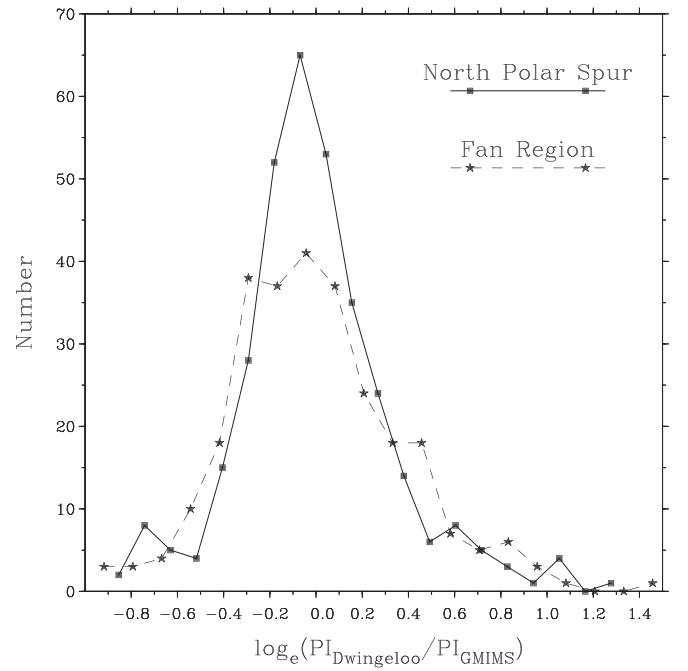


Figure 9. Histograms showing the ratio between Dwingeloo polarized intensities and GMIMS polarized intensities at 1411 MHz. A threshold is set for both surveys at $PI = 0.1$ K. The quantity plotted is $\log_e(PI_{Dwingeloo}/PI_{GMIMS})$.

Table 3
Selected Bands for Internal Spectrum Consistency Investigation

Band	Frequency Range (MHz)	Center Frequency (MHz)	Width (MHz)
1	1289.1–1322.3	1305.7	33.2
2	1322.3–1355.4	1338.9	33.2
3	1355.4–1418.2	1386.8	62.8
4	1418.2–1451.4	1434.8	33.2
5	1451.4–1483.3	1467.3	32.0
6	1483.3–1521.2	1502.3	37.9
7	1605.3–1653.8	1629.6	48.5
8	1653.8–1691.7	1672.8	37.9
9	1691.7–1733.2	1712.4	41.4

in nine frequency bands that were relatively free of RFI—details are given in Table 3. Within each band, individual channels are deleted due to RFI. Consequently the bands do not appear to be evenly spaced, and they appear to have different widths in frequency. There is a significant gap between 1521 and 1605 MHz where the RFI was particularly severe.

All-sky maps were made in the nine frequency bands. Since the sky minimum was removed from the total-intensity data by basketweaving, we could not compute the absolute spectral index. Instead, we computed T-T plots between pairs of frequencies over selected areas. In this experiment, where the two input frequencies are different, the slope of the T-T plot gives the temperature spectral index, β , in that frequency range, where $T_B \propto \nu^\beta$. The differential T-T plot method is unaffected by zero level errors.

Our primary test was made using the Cygnus-X area. In this complex region, the line of sight passes along the local spiral arm (Wendker et al. 1991). There are many H II regions in Cygnus X (Knödlseder 2000; Gottschalk et al. 2012), so there is a large amount of thermal emission. This region shows

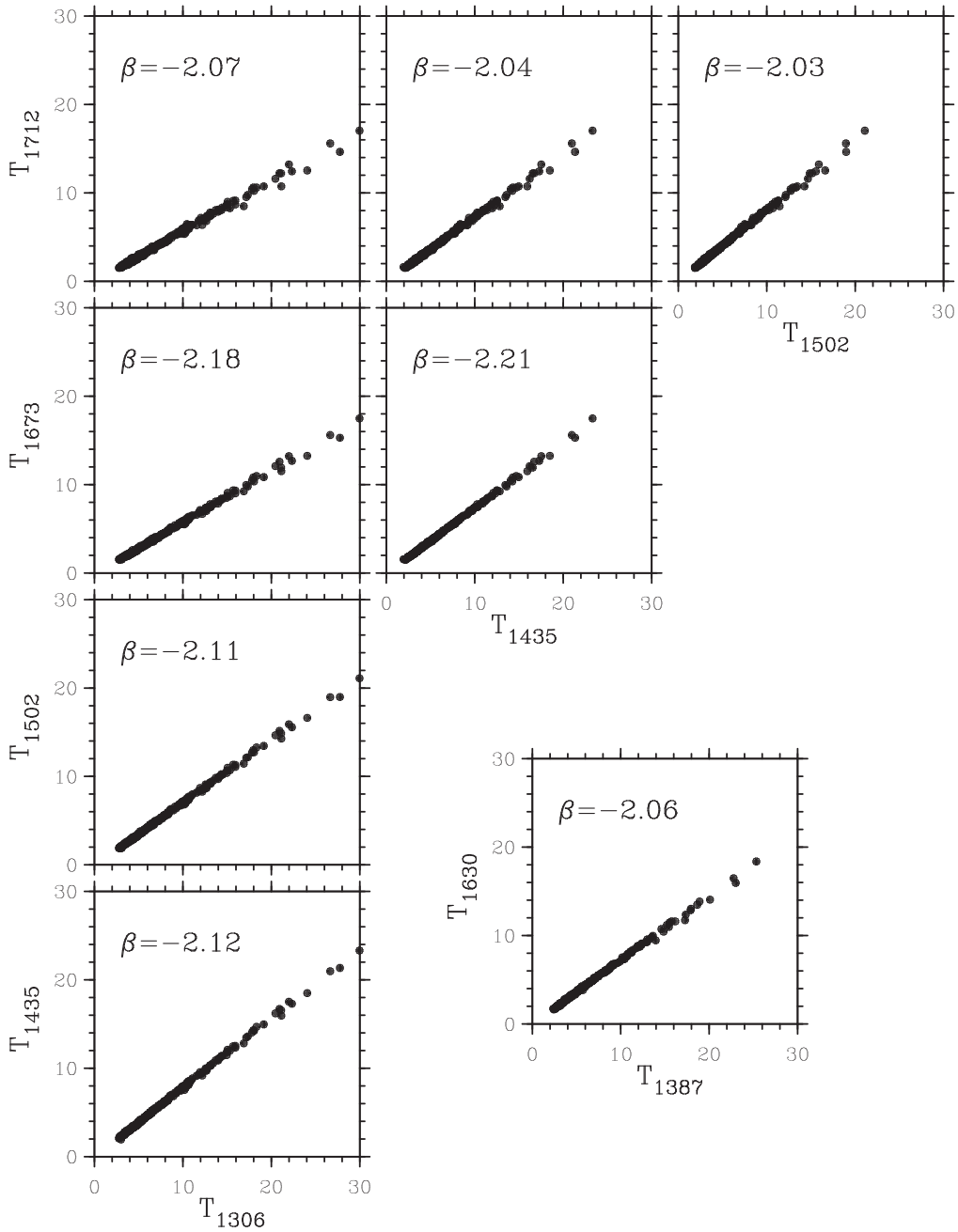


Figure 10. T-T plots made from 312 independent data points in the Cygnus-X area, covering an area of 78 square degrees defined by $75^\circ \leq \ell \leq 86.5^\circ$, $-2^\circ \leq b \leq 4^\circ$. The derived temperature spectral index, β , is shown in each plot. See the text for details.

$\beta \approx -2.4$ in the spectral index map of Reich & Reich (1988), computed between 408 and 1420 MHz. This is a lower value of β than the surroundings, indicating a mix of thermal and nonthermal emission. Xu et al. (2013) demonstrated that the thermal emission in Cygnus X is superimposed on a spatially nearly uniform background of nonthermal emission. We therefore expect the *differential* spectral index, as derived from our T-T plots, to be very close to $\beta = -2.1$, the value for optically thin thermal emission. T-T plots between the lower frequency channels and the upper channels did indeed produce values of β near -2.1 , and we concluded that we could use this region as a calibrator. T-T plots that involved channels 4, 5, and 6, at frequencies near 1500 MHz, produced results that implied that intensity scales of these bands were slightly too low. We adjusted data in channels 4, 5, and 6 upwards by

factors of 1.04, 1.05, and 1.05, respectively. Figure 10 shows T-T plots from eight pairs of frequencies over Cygnus X, after this adjustment to the central channels. Weighting the eight derived values of β by the frequency interval of each determination, we derived spectral indices for Cygnus X of $\beta = -2.10$ with a scatter of ± 0.08 .

We then proceeded to derive T-T plots over an area of intense emission near the Galactic center, just off the Galactic plane, where we expect the emission to be predominantly nonthermal, with a steeper spectrum. The T-T plots are shown in Figure 11 (after adjustment of central frequency channels). Averaging using the same weighting as above, we obtained $\beta = -2.50 \pm 0.09$.

These results are highly consistent, considering that many of these T-T plots are made over small frequency ranges. From

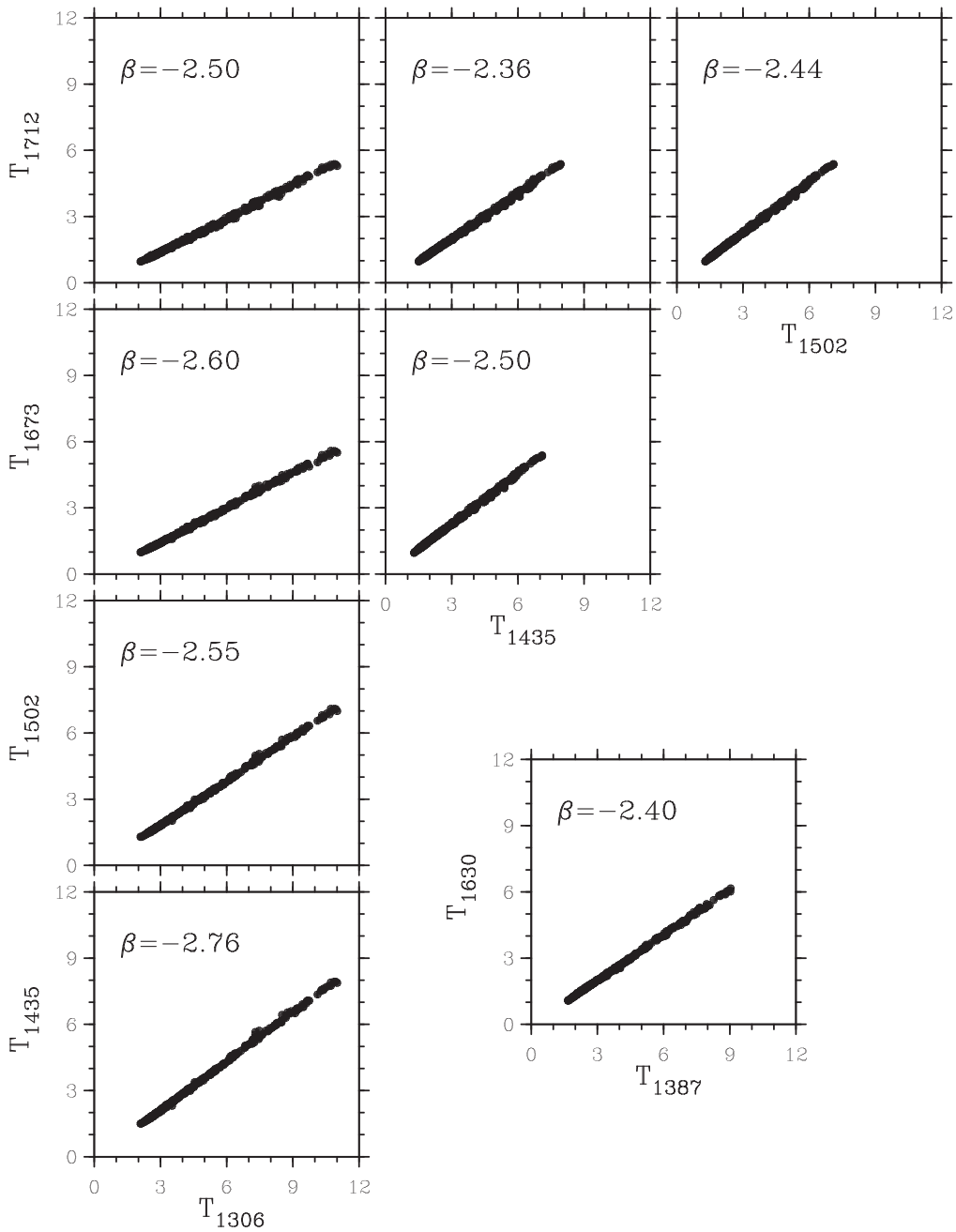


Figure 11. T-T plots made from 384 independent data points in the vicinity of the Galactic center, covering an area of 96 square degrees defined by $2^\circ \leq \ell \leq 13.5^\circ$, $2.5^\circ \leq b \leq 10^\circ$. The derived temperature spectral index, β , is shown in each plot. See the text for details.

this experiment, we conclude that the intensity scale is well determined across the band within a few percent. If the error in the intensity scale between 1306 and 1712 MHz was 3%, that would produce a change in β outside the range of values shown in Figures 10 and 11. We conclude that the probable error in relative intensities within the band is $\pm 2\%$, after the small adjustment of about 5% to frequencies near band center. We note that 5% is within the estimated overall error in our intensity scale (see Section 4.4). Examining Figure 2 we see that there are departures of this order of magnitude of the calculated aperture efficiency from the fitted second-order polynomial, especially at 1550 MHz, and we suggest this may be responsible for the scale discrepancy detected in the middle of the band. T-T plots involving data at 1550 MHz would have

provided a test of this hypothesis, but because of RFI, we could not make a useful total-intensity map at that frequency.

4.3. Reevaluation of the Angle Calibration

Comparison of polarization angle was possible with other data only in the vicinity of 1400 MHz: no surveys have been made at other frequencies in our band. Comparison with the single-frequency survey of Wolleben et al. (2006) showed a difference in polarization angle of $\sim 20^\circ$. That survey was calibrated using the 1411 MHz Dwingeloo data (Brouw & Spoelstra 1976); as expected, a direct comparison of the new data with the Brouw & Spoelstra (1976) data at 1411 MHz indicated a very similar angle offset. We had no a priori way of

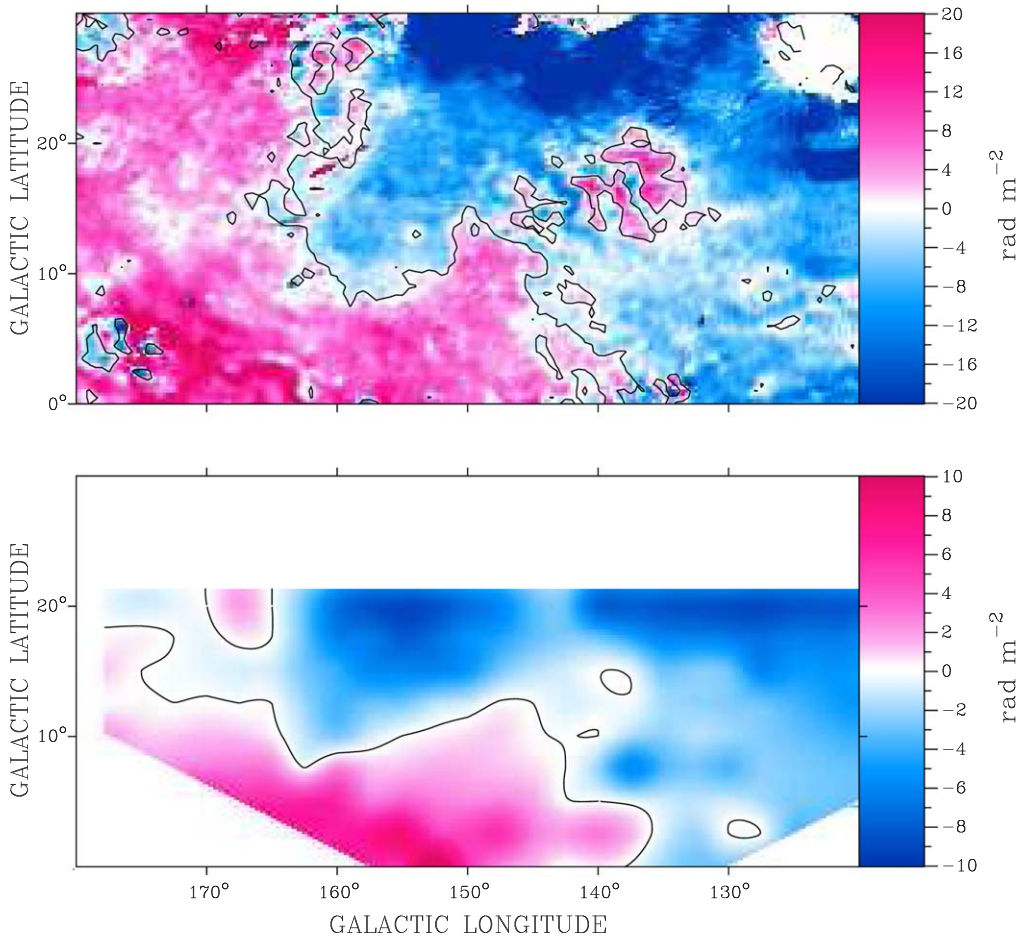


Figure 12. Top: GMIMS Moment 1 image over the Fan Region derived from the present survey, covering 1280–1750 MHz. The white region at the top right is the area north of decl. 87° where observations could not be made. Bottom: RM derived by Spoelstra (1984) from data between 408 and 1411 MHz over the same region. The bottom panel is based on data from Brouw & Spoelstra (1976) and is confined to the area covered by Figure 2 of Spoelstra (1984; calculated from the undersampled Dwingeloo data). The single contour shown in each image corresponds to 0 rad m^{-2} . Note that the range of the color scale in the bottom panel is half that used in the top panel.

establishing which, if any, of the three surveys was correct, but in this section we develop and apply a new angle calibration technique based on the Fan Region.

The Fan Region is an area where polarization angle changes very slowly with frequency, a fact well established from earlier polarization surveys. In Figure 12 we show a comparison of results derived from the new Faraday cube with a map of RM from Spoelstra (1984). The lower panel shows Spoelstra’s result, the RM computed from the Dwingeloo data, made by fitting observed polarization angle as a function of wavelength squared (as in Equation (4)) to narrowband measurements of polarization angle at 408, 465, 610, 820, and 1411 MHz. The upper panel shows the first moment computed from our Faraday cube, using the equations presented in Section 5. In the Fan region, where the Faraday depth structure is very simple, the first moment of Faraday depth is essentially equal to the “RM” value that would be calculated from our data by fitting polarization angle, χ , as a function of λ^2 . The two plots in Figure 12 are therefore quite comparable, and they are indeed strikingly similar. The line of zero RM in the Dwingeloo data corresponds closely to the line of zero first moment in our data, and the two data sets are correlated: where the FD is positive the RM is positive, and *vice versa*.

How reliable is this comparison? Our survey is fully sampled in frequency and angle, and the image shown in Figure 12

comprises 7200 independent data points. In contrast, the Dwingeloo observations are sparsely sampled in frequency and angle: the RM plot in Figure 12 is defined by only 227 data points. Nevertheless, the polarization structure in the Fan Region is very simple, changing quite slowly with sky position, and Faraday depths are low, so we consider the Dwingeloo RM values in Figure 12 to be a reliable representation of Faraday depth in the Dwingeloo frequency range.

Figure 13 shows a comparison of the mean FD values (first moment of the FD spectrum) point by point with the corresponding RM values over the area $120^\circ < \ell < 170^\circ$, $0^\circ < b < 20^\circ$. The two data sets are strongly correlated, but the GMIMS FD values are larger than the Dwingeloo RM values. The plotted line in Figure 13 has a slope of 2; this not a fitted line, but examination of the figure shows that it approximately represents the data. We avoid presenting a fit to these data points because we do not want to over-interpret this result (and the appearance of the plot changes slightly depending on the exact area from which data points are selected).

The most straightforward interpretation of Figure 13 is that the Dwingeloo data, covering 408–1411 MHz, mostly represent the nearby emission, because polarization horizon effects at those low frequencies, where beamwidths are large, confine the observations to the nearby magneto-ionic medium. The GMIMS FD data,

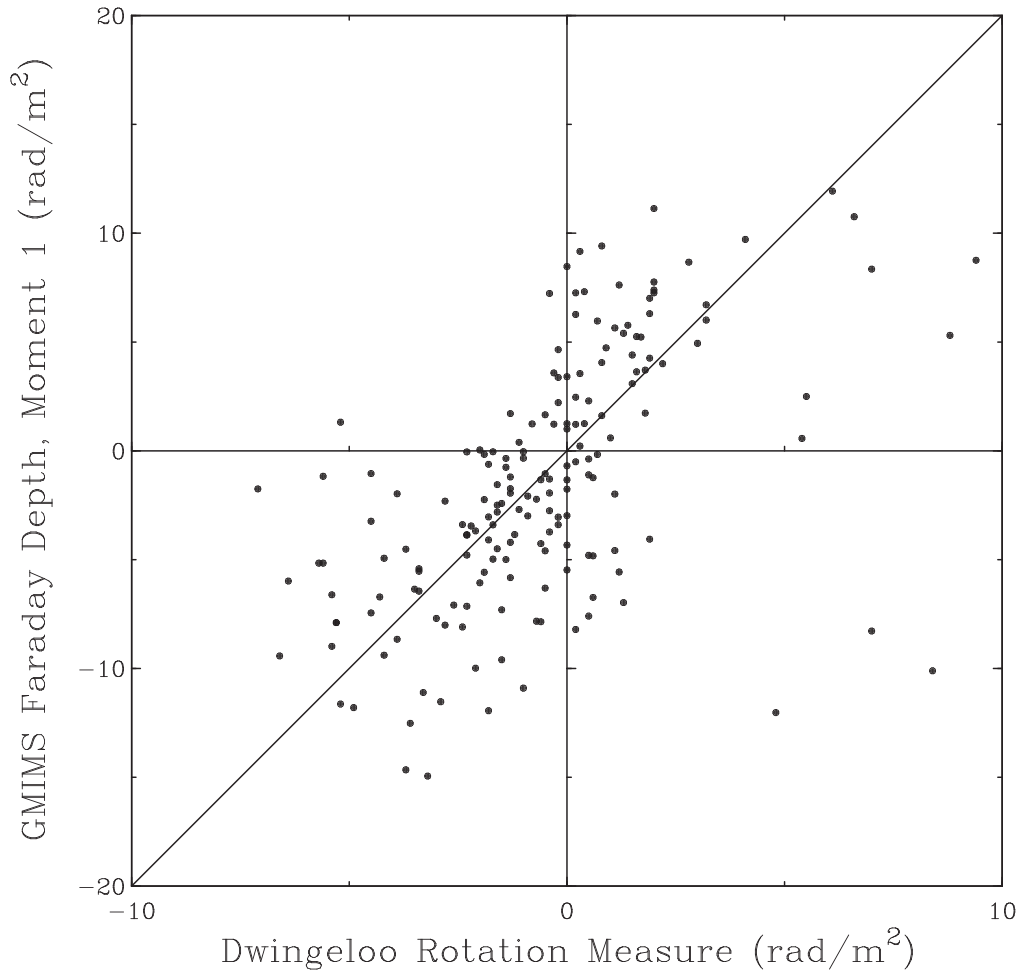


Figure 13. GMIMS Moment 1 values plotted against Dwingeloo RM values in the Fan Region. The plot covers the area $120^\circ < \ell < 170^\circ$, $0^\circ < b < 20^\circ$. The diagonal line has slope of 2; it is not a fit to the data. There are 185 data points in this plot, the number of Dwingeloo observations. (Note that this plot covers a slightly smaller area than the comparison in Figure 12.)

covering the frequency range 1280–1750 MHz, are sensitive to the magneto-ionic medium over a greater range of distance. Polarized emission from larger distances is likely to suffer more Faraday rotation than is experienced by local emission. Detailed interpretation of this result is beyond the scope of this paper; interpretation will be easier when polarization data that are fully sampled in the low-frequency range become available for the Fan region from surveys presently underway with DRAO telescopes.

The comparisons that we have made suggest that there is a specific area within the Fan Region where there is no, or very little, Faraday rotation between 408 and 1750 MHz (and, of course, at any higher frequency). This suggests that this area can be useful for calibration of polarization surveys in the Northern sky. We have put this into practice to re-calibrate the polarization angle for our survey. For this purpose, we adopt the *K*-band (23 GHz) data from WMAP (Bennett et al. 2013) as the calibration standard.

Figure 14 covers the same area as Figure 12, and shows the contour of zero Faraday depth. Rectangular boxes define three regions that lie along that contour, chosen to lie below $b = 15^\circ$ to capture the highest polarized intensity from the Fan region. In Table 4 we compare polarization angles in these three regions from the present data (designated as GMIMS), the data of Wolleben et al. (2006; DRAO 2006), and Bennett et al. (2013; WMAP). The GMIMS angles listed in Table 4 were

computed over the entire survey band, 1280–1750 MHz, removing the range 1520–1605 MHz where the data are severely affected by RFI. For each area, and each data set, we present the average polarization angle in that area, followed by a number in parentheses, which is the rms of the angle values in that area. In the case of GMIMS angles, the rms is calculated over all frequencies in the survey. Taking all three regions together, the average angle for the GMIMS data is -25° , and the distribution of values has an rms of 8° . We take the latter value as our estimate of the measurement error of angle in the survey (see Section 4.4).

The conclusion from inspection of Table 4 is that the GMIMS angles differ from the WMAP angles by $21.1 \pm 9.7^\circ$, and that our angle calibration based on 3C 286 is in error by this amount. Taking this result to one significant figure, we have added 20° to our polarization angles and re-calculated the *Q* and *U* data. The Faraday depth cube was completely unaffected by this operation because the same angle offset was applied to all frequency channels. The systematic error of WMAP polarization angles is 1.5° , plus an error up to 1° dependent on polarized intensity (Bennett et al. 2013). In the Fan Region, this error is likely to be $\sim 0.3^\circ$ (J. Weiland 2020, private communication). These errors are small compared to the errors in our data.

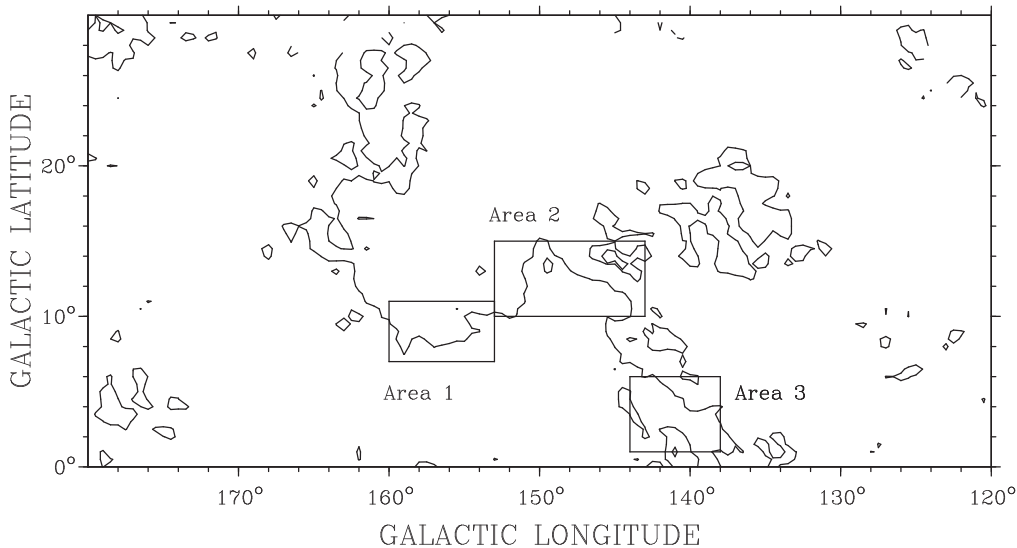


Figure 14. The area of the Fan Region, showing the contour of zero Faraday depth (from our Moment 1 data, as shown in Figure 12). Superimposed are outlines of three regions chosen for use in the calibration of polarization angle. See the text for details.

Table 4
Fan Region Polarization Angles

Area	Range in Longitude (degrees)	Range in Latitude (degrees)	Area (Square degrees)	WMAP PA ^a (deg)	GMIMS PA ^a (deg)	DRAO (2006) PA ^a (deg)
1	153–160	7–11	28	−3.5 (5.0) ^b	−24.5 (5.9)	−3.4 (3.5)
2	143–153	10–15	50	−6.2 (4.5)	−29.4 (9.2)	−2.3 (7.0)
3	138–144	1–6	30	−1.2 (3.4)	−19.3 (4.3)	3.1 (2.3)
All			108	−4.1(4.8)	−25.2(8.4)	−1.1 (5.8)

Notes.

^a All polarization angles are in the astronomical reference system, with zero at the Galactic north pole increasing to the east.

^b Each angle value is followed by a number in parentheses, which is the rms calculated from the angle values in that area.

The Fan Region is unique as an angle calibrator for single-antenna polarization observations. The Fan Region has high polarized intensity, and its polarization angle is unchanging from 408 MHz to high frequencies. No other region in the Northern sky has this combination of properties.

4.4. Error Analysis

We discuss errors in polarized intensity and polarization angle separately.

The noise on Q and U images, measured in low-signal regions of images made with a channel width of 1.18 MHz, is 45 mK. From the known system temperature and integration time, we expect a noise level of 41 mK rms (calculated following the method of McConnell et al. 2006). The noise on the Faraday depth cube is lower, 3.3 mK, because the entire bandwidth participates in the determination of each data value in this cube. The theoretical estimate is 2.4 mK, calculated on the basis of the RFI-free bandwidth that has been used in computing the Faraday depth cube.

The error in our knowledge of the flux density of Cygnus A is 5% (derived from the errors quoted by Baars et al. 1977). Beyond this is the possibility of error in the determination of aperture efficiency, arising in the actual measurements; this is 3% (Du et al. 2016). There is definitely additional error that

must be considered, from the application of the calibration data to individual scans and the processes, such as basketweaving, that we have applied to the data. We estimate this error as 5%. Combining these errors, the probable error in polarized intensities is 8%.

In Section 4.2 we investigated the relative accuracy of the intensity scale internal to the survey on the basis of total-intensity data, and reached the conclusion that the internal scale has a probable error of 2%.

In Section 4.3 we presented results for polarization angle in the Fan Region. The scatter of measurements over 108 square degrees is 8° rms (Table 4). This value does not reflect thermal noise; it incorporates, and is dominated by, the systematic and random effects that influence the determination of angle. Although the sky directions involved are close together, that does not mean that the observations were close in time. In fact, our observation technique ensured that measurements of neighboring points were well spread out in time, and the basketweaving process brought a large number of observations, made over a long time period, to bear on the determination of every data point. We therefore adopt 8° as the probable error in angle of our data. This includes a small contribution arising from the fact that we have not corrected for ionospheric Faraday rotation (see Section 3.10). To this error we must add

Table 5
Characteristics of Published Survey Data

Frequency range, I , Q , and U	1280–1750 MHz
Channel width	1.1804 MHz
Available data formats	Galactic coordinates, fits and healpix
Noise, Q and U images (single channel)	45 mK
Noise, I images (50 MHz band)	20 mK
Probable error, amplitude scale	8%
Probable relative error, internal intensity scale	2%
Probable error, polarization angles	8°
Systematic error, calibration of polarization angle	1.5°
Coverage of Faraday cube	$\pm 500 \text{ rad m}^{-2}$
Channel width in Faraday cube	5 rad m^{-2}
Largest detectable Faraday depth	$\sim 2 \times 10^4 \text{ rad m}^{-2}$
Resolution in Faraday depth	150 rad m^{-2}
Largest measurable RM Structure	110 rad m^{-2}
Sensitivity in Faraday depth cube	3.3 mK (rms) of polarized intensity

1.5° for the systematic error in our calibration of angle using the WMAP data.

The sky was not uniformly sampled by our observing technique. The observing scheme, described in Section 2.2, of half the scans terminating at decl. 60° and half terminating at 87°, was designed to spread the available observing time more optimally over the sky. Despite this, sampling at high decl. was still more thorough than sampling at low decl., and we might expect greater sensitivity at high decl. Nevertheless, it was difficult to discern any systematic improvement in survey data at high decl., possibly because of systematic effects. We note that the principal product of the survey, the Faraday depth cube, is derived from angle data. As pointed out above, uncertainties in angle data are dominated by systematic errors, not by thermal noise.

5. Results

In this section we present a few results from the survey. We describe a check of the quality of the Faraday cube, and show one example that illustrates some of the scientific potential of the data. Table 5 gives details of the published data.

The spectral moments of the Faraday cube (Dickey et al. 2019) provide a very succinct portrait of multichannel polarization data, and we use them here. The zero moment is the total polarized intensity integrated over the full range of ϕ ; it is defined as

$$M_0 \equiv \sum_{i=1}^n T_i \Delta\phi, \quad (14)$$

with units K rad m^{-2} , where T_i is the polarized intensity at channel i , and $\Delta\phi$ is the width of each of the n channels of the Faraday spectrum contributing to the sum. The first moment is the intensity-weighted mean of the Faraday depth. In Faraday simple directions, this is the same as the peak Faraday depth. The first moment is

$$M_1 \equiv \frac{\sum_{i=1}^n T_i \phi_i}{\sum_{i=1}^n T_i}, \quad (15)$$

with units rad m^{-2} . We excluded Faraday depth channels beyond $\pm 500 \text{ rad m}^{-2}$ in the moment calculations to avoid

contamination by spurious peaks (see Section 3.11), and excluded channels having polarized intensity below 0.04 K (0.01 K higher than the CLEAN threshold). For each pixel, Faraday depth peaks with polarized intensities lower than 15% of the primary peak in that spectrum were also excluded.

Figure 15 shows Stokes I at 1497 MHz and the zero moment map. Figure 16 presents a map of polarization angle, χ , at 1497 MHz and first moments computed from the Faraday cube. Inspection of Figure 16 shows some areas where the Faraday depth is significantly nonzero. This discovery was the basis of the first scientific paper from this survey: Wolleben et al. (2010a) demonstrated the association of strong features in Faraday depth with a large HI bubble.

Close inspection of the images in Figures 15 and 16 reveals some artifacts near the southern survey limit. These arise from imperfect removal of ground emission and other instrumental effects. The artifacts vary with frequency and position, and are very difficult to quantify. They are confined within 5° of the southern limit. The sky at the southern limit of the survey, decl. -30° , was observed at an elevation of only 11°, above an uneven, mountainous horizon. We anticipated that correction for ground radiation would be difficult under these circumstances, but we chose this southern limit in order to maximize overlap with GMIMS surveys of the southern sky (e.g., Wolleben et al. 2019). Readers should exercise caution in using survey data between decl. -25° and -30° .

5.1. Quality of the Faraday Cube

In Figure 17 we present χ - χ plots, comparing polarization angles at two frequencies within this survey. The left column compares observed polarization angles at 1394 and 1725 MHz. In the right column, we derotated the angles at both frequencies as

$$\chi_{\text{derot}} = \chi_0 - \phi\lambda^2, \quad (16)$$

where χ_0 is the raw angle and ϕ is the Moment 1 Faraday depth at each pixel. The rows in Figure 17 contain the whole sky, the North Polar Spur, and the Fan Region. In the raw χ - χ plots, the agreement between polarization angles is already good, as expected because there is relatively little Faraday rotation, given the fairly small Faraday depths and short wavelengths in this survey. However, there are notable deviations from the 1:1 line that are especially evident in the North Polar Spur and Fan Region. In particular, there are a significant number of points at which the 1727 MHz angles are smaller by $\pi/8$ radians than the 1395 MHz angles in the North Polar Spur and at which the 1727 MHz angles are larger by a comparable amount than the 1395 MHz angles in the Fan Region, especially near χ (1395 MHz) $\approx -\pi/8$.

The derotation process brings most of the points for which the angles are discrepant from 1:1 back in line. The histograms and associated statistics in Figure 18 show that the derotation process also reduces the scatter in all three samples: the distribution of derotated polarization angles is more centrally peaked and narrower than the distribution of raw polarization angles, and the standard deviations of the distributions are reduced by 18%–35%. Moreover, in both Figures 17 and 18, it is evident that the derotated data have fewer points in which the angles differ by $\sim\pi/4$ or, equivalently, are far from the 1:1 lines in Figure 17. We interpret this as an indication of the

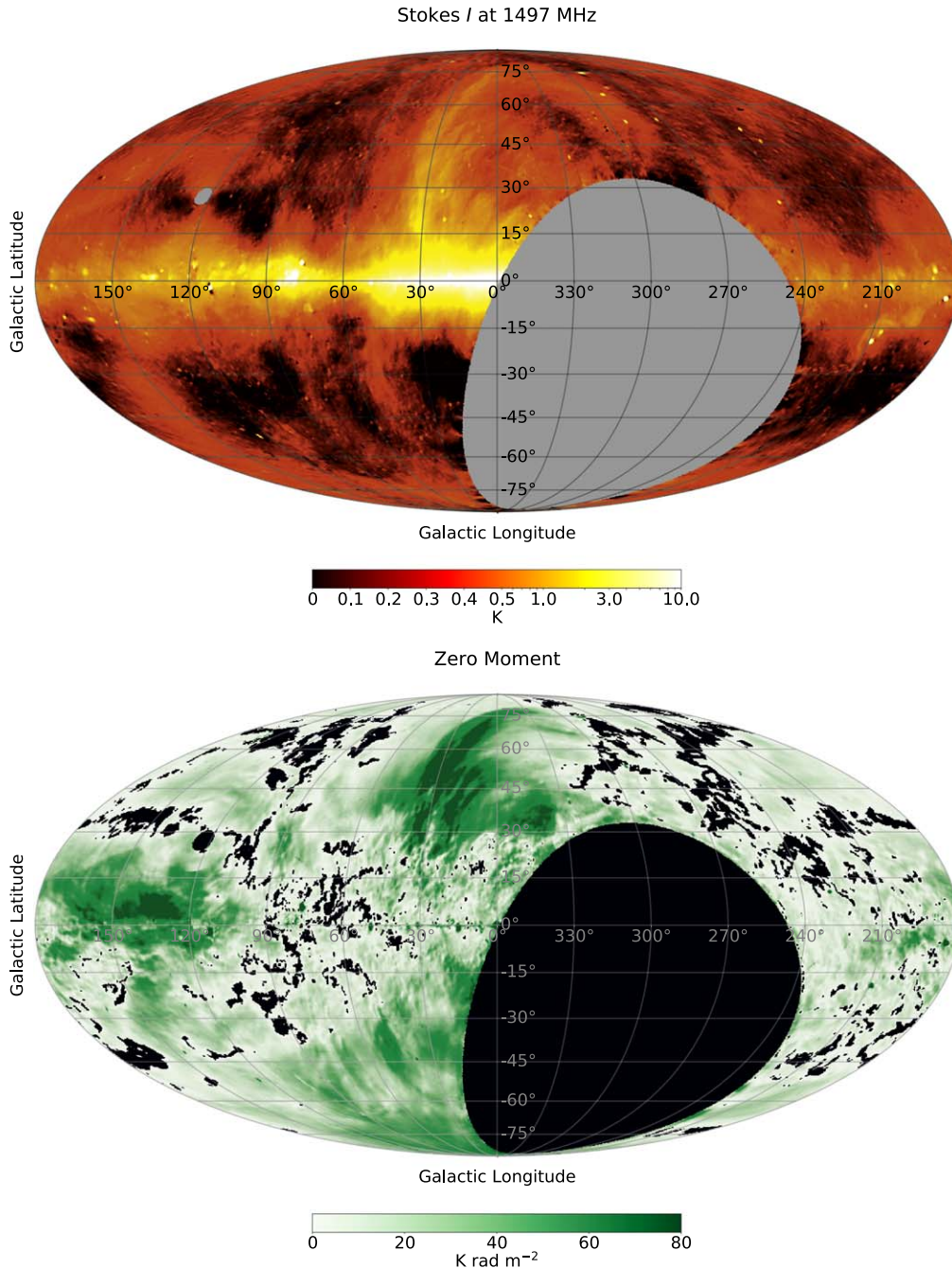


Figure 15. Top: total intensity at 1497 MHz. The intensity scale of this image is correct, but the zero level is not (see the text). Pixels outside the survey limits are gray. Bottom: zero moment computed from the Faraday cube, using the equations of Dickey et al. (2019). Pixels with insufficient data for the moment calculation, and those outside the survey area, are black. Both images are plotted in Galactic coordinates in Mollweide projection.

Faraday simplicity of the data in this band as well as a check on the efficacy of the RM synthesis procedure.

If the observed Faraday rotation were idealized such that χ was a straight line as a function of λ^2 , we would expect this derotation process to produce perfect agreement across frequencies. In this case, the Faraday synthesis process would have been unnecessary in the first place, and we could have simply measured $\text{RM} = d\chi/d\lambda^2$. We do not observe this: there is noticeable scatter about the 1:1 line. This is not surprising: it is simply a confirmation that the interstellar medium is not Faraday simple. We take the tight relationship of polarization angle across the band, in particular after derotating, as a check

on the internal consistency of the polarization angle measurements in this survey.

5.2. The H II Region Sharpless 2-27

As an example of insights to be gained from the Faraday depth cube, we discuss FD spectra in the direction of the H II region Sharpless 2-27 (which we refer to as S27). S27, at $(\ell, b) = (6^\circ.3, 23^\circ.6)$ is a large H II region, $\sim 10^\circ$ in extent, excited by the star ζ Oph whose distance is 180 pc (Gaia Collaboration et al. 2016, 2018). Figure 19 shows the object in H α from the data of Finkbeiner (2003), and in our data at a Faraday depth of -55 rad m^{-2} . Figure 20 shows the Faraday depth spectra at two

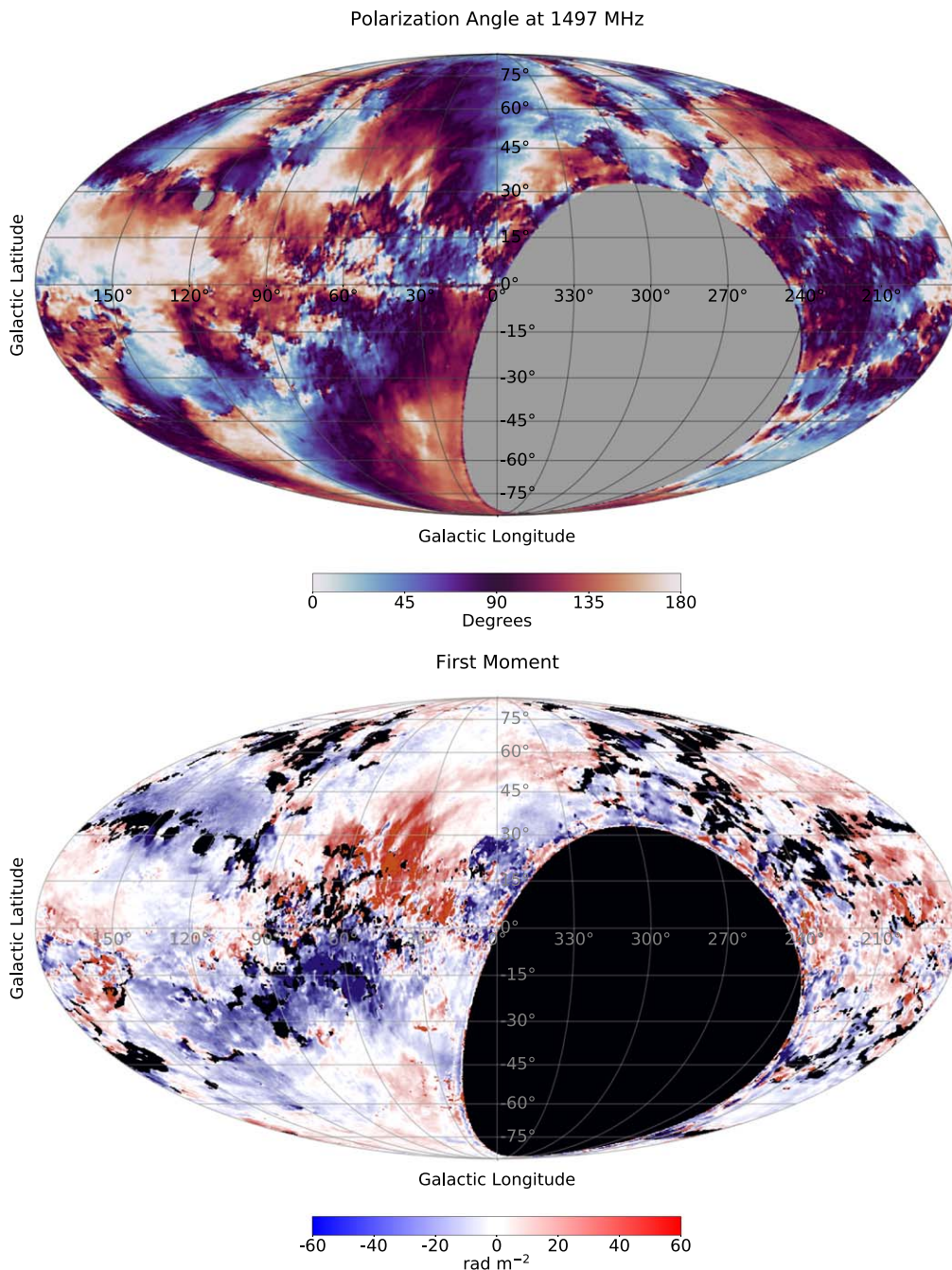


Figure 16. Top: polarization angle at 1497 MHz. Pixels outside the survey limits are gray. Bottom: first moment computed from the Faraday cube, using the equations of Dickey et al. (2019). Pixels with insufficient data for the moment calculation, and those outside the survey area, are black. Both images are plotted in Galactic coordinates in Mollweide projection.

points, one on S27 and one in a nearby direction off the H II region.

Thomson et al. (2019) have analyzed data from the GMIMS 300–480 MHz survey (Wolleben et al. 2019) in the direction of S27. At those low frequencies, the H II region totally depolarizes background emission, and the Faraday spectrum reveals details of the synchrotron emission generated in the foreground column. It is evident from Figure 20 that S27 has strong Faraday effects in the 1280–1750 MHz band as well. Here we present only an outline interpretation of the data. We will present a full analysis of our data in this direction in a forthcoming paper (A. Ordog et al. 2021, in preparation).

In the frequency range of the present work, background emission is strongly depolarized and Faraday rotated by S27. The off-source FD spectrum in Figure 20 peaks at a polarized intensity of 0.37 K RMSF^{-1} , and there is only one peak, at about $+15 \text{ rad m}^{-2}$. The on-source spectrum shows two peaks, at $+22$ and -190 rad m^{-2} , and polarized intensity reaches no higher than 0.09 K RMSF^{-1} . We interpret this spectrum as showing foreground emission from the 165 pc path²⁶ between S27 and the telescope (the peak at positive Faraday depth), and background emission Faraday rotated on passing through S27

²⁶ The distance, 180 pc, to the exciting star minus the 15 pc radius of S27.

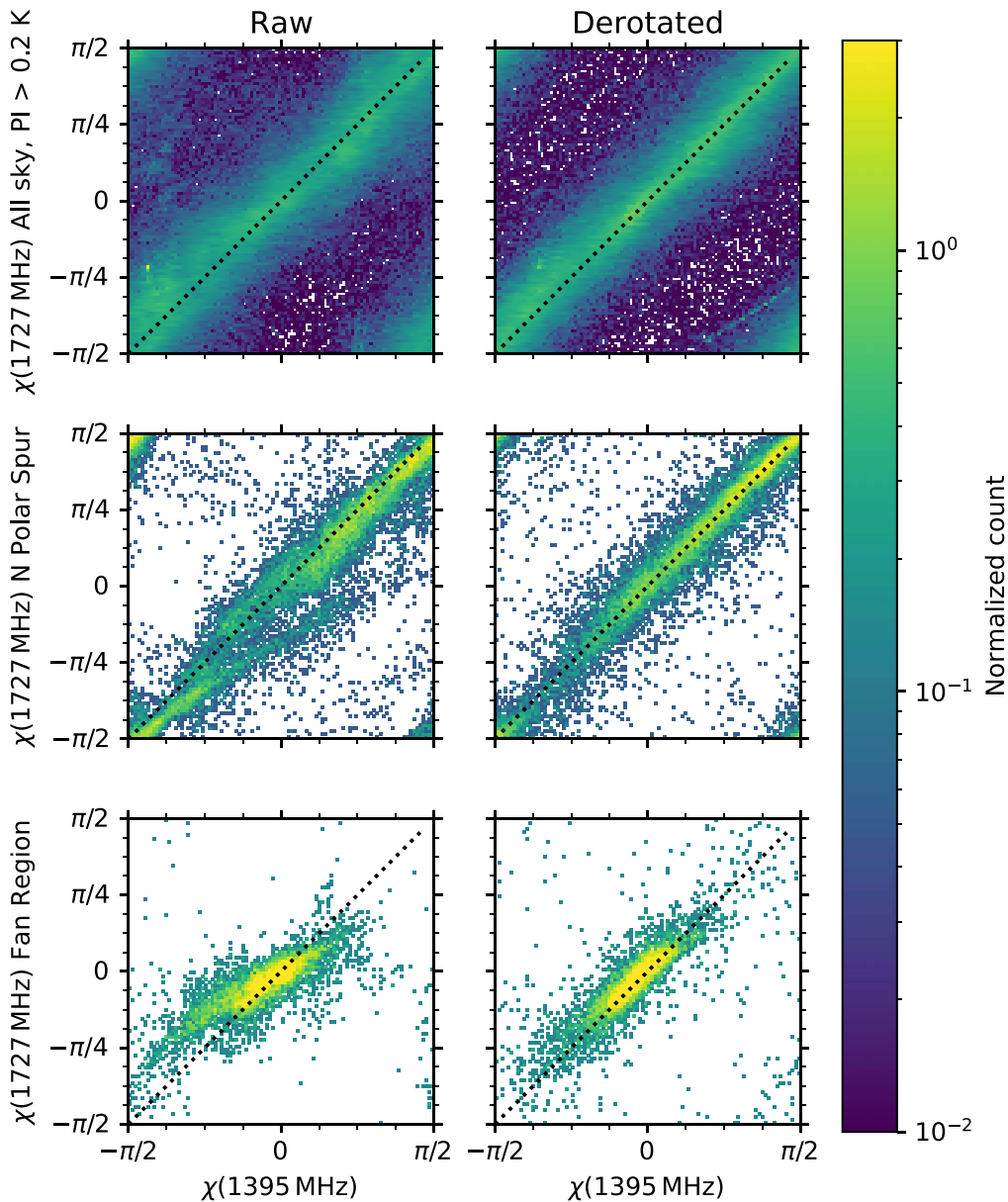


Figure 17. Polarization angle at 1725 MHz plotted point by point against polarization angle at 1394 MHz. Top row: the entire survey, for points where the polarized intensity exceeds 0.2 K. Middle row: North Polar Spur. Bottom row: Fan Region. Left column: polarization angles as observed. Right column: the same scatter plot but the angles at 1394 and 1725 MHz have been rotated by angle $-\phi \lambda^2$ where ϕ is the Faraday depth deduced from the first moment map.

(the peak at negative Faraday depth). Faraday rotation through S27 was identified by Harvey-Smith et al. (2011) by examination of RMs of background sources seen through the object using RMs from the catalog of Taylor et al. (2009). The two sources from that catalog closest to $(\ell, b) = (8^\circ, 23^\circ 5')$ have an average RM of -217 rad m^{-2} . The average RM of six sources within a 3° circle around that position is -162 rad m^{-2} . These values compare well with the Faraday depth at that position in our data.

6. Conclusions

We have described observations and data processing that have yielded Stokes parameters I , Q , and U over the Northern sky, between decl. limits of -30° and $+87^\circ$, covering 72% of the sky; 95% of full Nyquist sampling has been achieved. Frequency coverage is 1280–1750 MHz. Although much of this frequency band lies outside the ranges allocated to radio

astronomy, the data loss to RFI is only $\sim 30\%$. This work was designed as a Faraday depth survey, not simply a polarization survey, and its most valuable published data product is a Faraday depth cube, covering $\pm 500 \text{ rad m}^{-2}$. We have achieved a sensitivity of 3 mK and a resolution in Faraday depth of 150 rad m^{-2} . However, our sensitivity to wide structures in Faraday depth extends only as far as 110 rad m^{-2} . Future plans for the GMIMS project include observations at lower frequencies. When coverage is extended down to 800 MHz, the resolution in Faraday depth will improve to $\sim 35 \text{ rad m}^{-2}$ with the same sensitivity to extended FD structures. We will then be able to identify wide structures in Faraday depth without ambiguity.

Users of the data should be aware that we have concentrated on an accurate depiction of the extended polarized emission. Furthermore, our observing technique is not ideal for the measurement of compact sources, and data on such sources

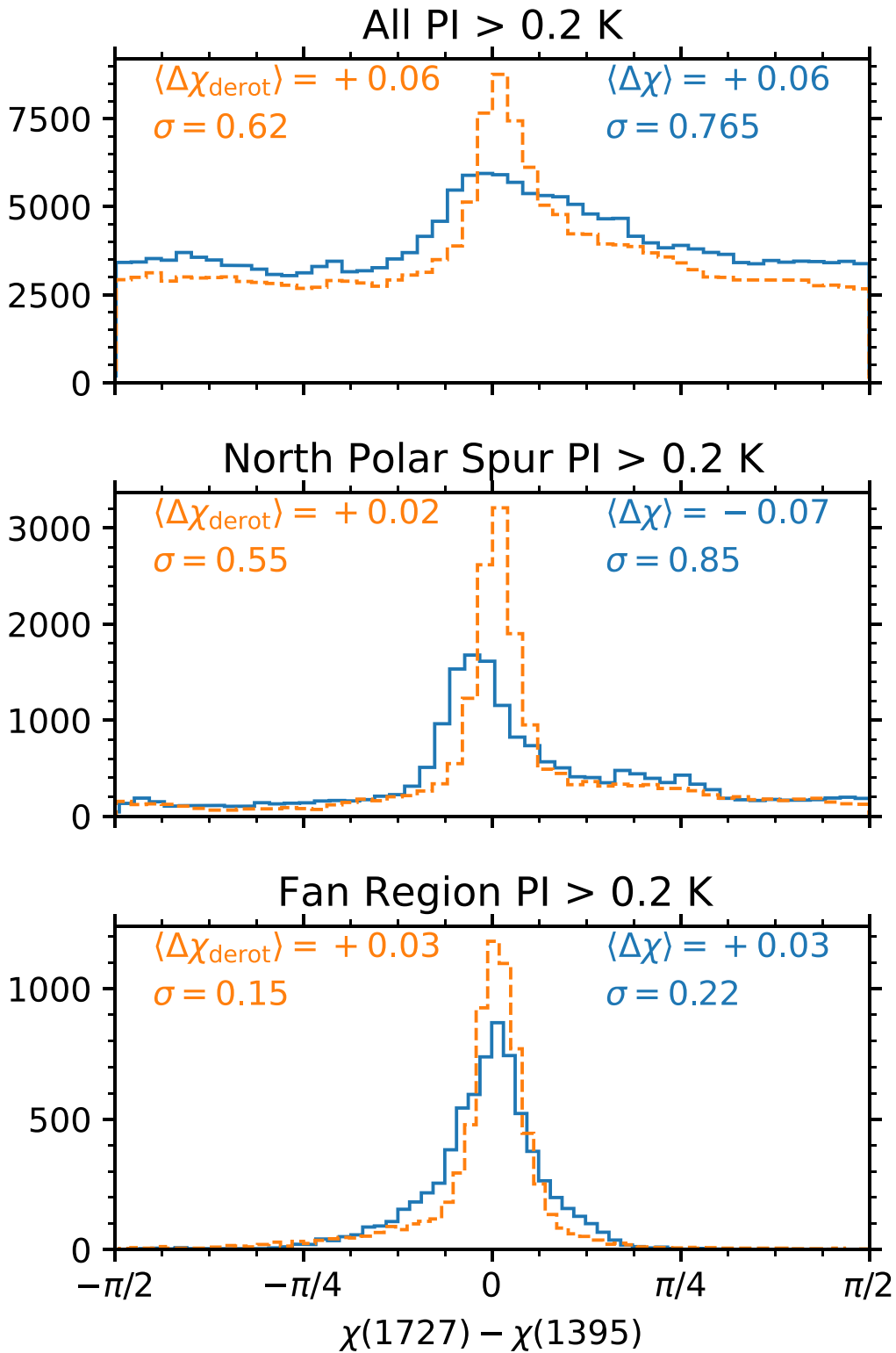


Figure 18. Histograms of the differences in polarization angle for the scatter plots of Figure 17. The mean, $\langle \Delta\chi \rangle$, and standard deviation, σ , for each histogram are indicated.

extracted from our survey should be treated with caution. We note, again, that basketweaving has removed the sky minimum from total-intensity images; any use of the total-intensity data must take this fact into account.

The survey has been calibrated against absolute standards of noise and the well-established flux density and spectrum of Cygnus A, and all data products are in units of absolutely

calibrated main-beam brightness temperatures. This was necessary because no comparable surveys were available as calibrators, except near 1400 MHz. All GMIMS surveys are (or will be) absolutely calibrated, and this allows accurate intercomparison and combination of data from different component surveys. Comparison with available total-intensity data near 1400 MHz demonstrates very satisfactory agreement

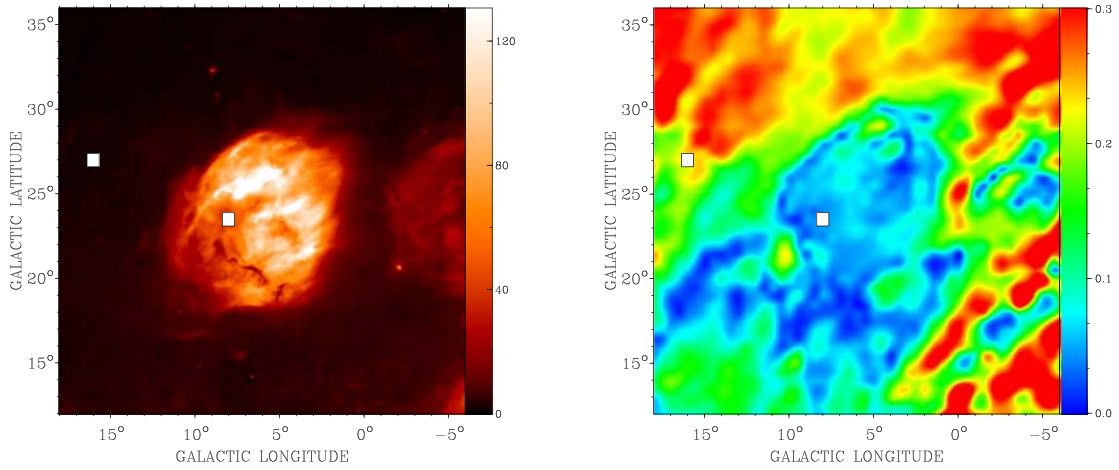


Figure 19. The H II region Sharpless 2-27. The left panel shows H α image in units of Rayleighs from the data of Finkbeiner (2003). The right panel shows polarized intensity at a Faraday depth of -55 rad m^{-2} in units of K RMSF^{-1} . Two white squares are superimposed on these images: these are the locations of the two Faraday spectra shown in Figure 20.

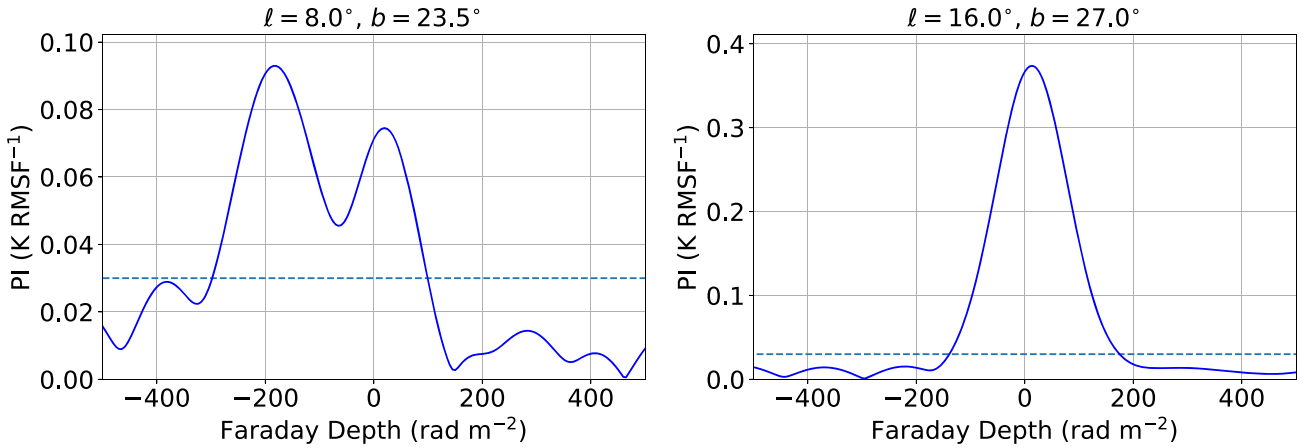


Figure 20. Faraday spectra at $(\ell, b) = (8^\circ, 23.5^\circ)$ and $(16^\circ, 27^\circ)$. The dotted line on each plot shows the clean limit, 0.03 K RMSF^{-1} .

of scales, within 5%. Comparison with available polarization data indicates agreement of the polarized intensity scale within 10%. The intensity scale within the 1280–1750 MHz passband is consistent within 2%. We have demonstrated a new technique for calibration of polarization angle using lines of sight in the Fan Region that we have identified as having zero Faraday rotation; we have calibrated our data using the WMAP 23 GHz data set. This technique can be applied to any polarization survey in the North, and will be used with future GMIMS surveys.

We encountered some difficulty with estimation of the ground contribution. In that regard our technique of making observations by moving the telescope in elevation is not ideal. The technique developed by Carretti et al. (2019) for the S-band Polarization All Sky Survey, scanning in azimuth, is superior, but the equatorial mounting of the Galt Telescope ruled that out as a possibility.

This is the second GMIMS survey to be published, following the 300–480 MHz survey of the Southern sky with the Parkes 64 m Telescope (Wolleben et al. 2019). The overlap between the surveys spans the decl. range -30° to $+20^\circ$, 42% of the sky. This overlap has already been exploited by Dickey et al. (2019) to compare the two surveys, and it has great future potential. Once again we find that a large fraction of the sky displays significant polarized emission at nonzero Faraday



depth. This was not apparent from polarization surveys at single frequencies, of course, and provides a rich opportunity for investigation.

The data presented here are available at the Canadian Astronomy Data Centre, at doi:21.0003.

We are indebted to Rob Messing for his skill in designing, building, and maintaining the receiver through the course of this project. We thank Xuan Du and Tim Robshaw for outstanding contributions to the determination of aperture efficiency of the telescope. Stasi Baran helped greatly with the observations. We thank Sean Dougherty for his support of this project. The Dominion Radio Astrophysical Observatory is a National Facility operated by the National Research Council Canada. Janet Weiland of Johns Hopkins University provided us with information on systematic errors in WMAP data. The Global Magneto-Ionic Medium Survey is a Canadian project with international partners. The participation of M.W., K.H.D., A.O., and A.S.H. was supported in part by the Natural Sciences and Engineering Research Council (NSERC). The work of A.S.H. and A.O. was also supported by the Dunlap Institute and the National Research Council Canada. The Dunlap Institute is funded through an endowment established by the David Dunlap family and the University of Toronto. B.M.G. acknowledges support from NSERC and the Canada Research Chairs program. J.L.H. is

supported by the National Natural Science Foundation of China (NNSFC grants 11988101 and 11833009) and the Key Research Program of the Chinese Academy of Sciences (grant QYZDJ-SSW-SLH021). This research has been enabled by the use of computing resources provided by WestGrid and Compute/Calcul Canada and the Centre for High Performance Computing in Cape Town, South Africa.

ORCID iDs

T. L. Landecker  <https://orcid.org/0000-0003-1455-2546>
 K. A. Douglas  <https://orcid.org/0000-0003-3320-2728>
 A. D. Gray  <https://orcid.org/0000-0002-2280-7644>
 A. Ordog  <https://orcid.org/0000-0002-2465-8937>
 J. M. Dickey  <https://orcid.org/0000-0002-6300-7459>
 A. S. Hill  <https://orcid.org/0000-0001-7301-5666>
 E. Carretti  <https://orcid.org/0000-0002-3973-8403>
 J. C. Brown  <https://orcid.org/0000-0003-4781-5701>
 B. M. Gaensler  <https://orcid.org/0000-0002-3382-9558>
 J. L. Han  <https://orcid.org/0000-0002-9274-3092>
 M. Haverkorn  <https://orcid.org/0000-0002-5288-312X>
 R. Kothes  <https://orcid.org/0000-0001-5953-0100>
 N. McClure-Griffiths  <https://orcid.org/0000-0003-2730-957X>
 D. McConnell  <https://orcid.org/0000-0002-2819-9977>
 W. Reich  <https://orcid.org/0000-0002-5313-6409>
 A. R. Taylor  <https://orcid.org/0000-0001-9885-0676>
 A. J. M. Thomson  <https://orcid.org/0000-0001-9472-041X>
 J. L. West  <https://orcid.org/0000-0001-7722-8458>

References

- Aller, H. D., & Reynolds, S. P. 1985, *ApJL*, **293**, L73
 Baars, J. W. M. 2007, *The Paraboloidal Reflector Antenna in Radio Astronomy and Communications* (Berlin: Springer)
 Baars, J. W. M., Genzel, R., Pauliny-Toth, I. I. K., & Witzel, A. 1977, *A&A*, **61**, 99
 Beck, R., Brandenburg, A., Moss, D., Shukurov, A., & Sokoloff, D. 1996, *ARA&A*, **34**, 155
 Bennett, C. L., Larson, D., Weiland, J. L., et al. 2013, *ApJS*, **208**, 20
 Boulares, A., & Cox, D. P. 1990, *ApJ*, **365**, 544
 Brentjens, M. A., & de Bruyn, A. G. 2005, *A&A*, **441**, 1217
 Brouw, W. N., & Spoelstra, T. A. T. 1976, *A&AS*, **26**, 129
 Brown, J. C., Haverkorn, M., Gaensler, B. M., et al. 2007, *ApJ*, **663**, 258
 Burn, B. J. 1966, *MNRAS*, **133**, 67
 Carretti, E., Haverkorn, M., Staveley-Smith, L., et al. 2019, *MNRAS*, **489**, 2330
 Costain, C. H. 1960, *MNRAS*, **120**, 248
 de Bruyn, A. G., & Brentjens, M. A. 2005, *A&A*, **441**, 931
 Dickey, J. M., Landecker, T. L., Thomson, A. J. M., et al. 2019, *ApJ*, **871**, 106
 Du, X., Landecker, T. L., Robishaw, T., et al. 2016, *PASP*, **128**, 115006
 Ferrière, K. M. 2001, *RvMP*, **73**, 1031
 Finkbeiner, D. P. 2003, *ApJS*, **146**, 407
 Gaia Collaboration, Brown, A. G. A., & Vallenari, A. 2018, *A&A*, **616**, A1
 Gaia Collaboration, Prusti, T., & de Bruijne, J. H. J. 2016, *A&A*, **595**, A1
 Gao, X. Y., Reich, W., Han, J. L., et al. 2010, *A&A*, **515**, A64
 Gibbins, C. J. 1986, *RaSc*, **21**, 949
 Gottschalk, M., Kothes, R., Matthews, H. E., Landecker, T. L., & Dent, W. R. F. 2012, *A&A*, **541**, A79
 Han, J. L. 2017, *ARA&A*, **55**, 111
 Han, J. L., Manchester, R. N., Lyne, A. G., Qiao, G. J., & van Straten, W. 2006, *ApJ*, **642**, 868
 Harvey-Smith, L., Madsen, G. J., & Gaensler, B. M. 2011, *ApJ*, **736**, 83
 Haslam, C. G. T., Wilson, W. E., Graham, D. A., & Hunt, G. C. 1974, *A&AS*, **13**, 359
 Haverkorn, M., Gaensler, B. M., McClure-Griffiths, N. M., Dickey, J. M., & Green, A. J. 2006, *ApJS*, **167**, 230
 Heald, G. 2009, in *Cosmic Magnetic Fields: From Planets, to Stars and Galaxies*, Vol. 259, ed. K. G. Strassmeier, A. G. Kosovichev, & J. E. Beckman, 591
 Heiles, C., & Haverkorn, M. 2012, *SSRv*, **166**, 293
 Helmboldt, J. F., Kassim, N. E., Cohen, A. S., Lane, W. M., & Lazio, T. J. 2008, *ApJS*, **174**, 313
 Hill, A. S., Joung, M. R., Mac Low, M.-M., et al. 2012, *ApJ*, **750**, 104
 Hill, A. S., Landecker, T. L., Carretti, E., et al. 2017, *MNRAS*, **467**, 4631
 Jaffe, T. R. 2019, *Galax*, **7**, 52
 Jaffe, T. R., Ferrière, K. M., Banday, A. J., et al. 2013, *MNRAS*, **431**, 683
 Jansson, R., & Farrar, G. R. 2012, *ApJ*, **757**, 14
 Kim, E.-J., Olinto, A. V., & Rosner, R. 1996, *ApJ*, **468**, 28
 Knödseder, J. 2000, *A&A*, **360**, 539
 Landecker, T. L., Reich, W., Reid, R. I., et al. 2010, *A&A*, **520**, A80
 McConnell, D., Carretti, E., & Subrahmanyan, R. 2006, *AJ*, **131**, 648
 Moss, D., & Sokoloff, D. 2019, *Galax*, **7**, 36
 Ng, T., Landecker, T. L., Cazzolato, F., et al. 2005, *RaSc*, **40**, 5014
 Padoan, P., & Nordlund, Å. 2011, *ApJ*, **730**, 40
 Purcell, C. R., Van Eck, C. L., West, J., Sun, X. H., & Gaensler, B. M. 2020, *RM-Tools: Rotation Measure (RM) Synthesis and Stokes QU-fitting*, Astrophysics Source Code Library, ascl:2005.003
 Reich, P., & Reich, W. 1986, *A&AS*, **63**, 205
 Reich, P., & Reich, W. 1988, *A&AS*, **74**, 7
 Reich, W. 1982, *A&AS*, **48**, 219
 Reich, W., Fürst, E., Reich, P., et al. 2004, *The Magnetized Interstellar Medium*, ed. B. Uyaniker, W. Reich, & R. Wielebinski, 45
 Reichart, D. E., & Stephens, A. W. 2000, *ApJ*, **537**, 904
 Robishaw, T., & Heiles, C. 2018, arXiv:1806.07391
 Spoelstra, T. A. T. 1984, *A&A*, **135**, 238
 Sun, X. H., Han, J. L., Reich, W., et al. 2007, *A&A*, **469**, 1003
 Sun, X. H., Landecker, T. L., Gaensler, B. M., et al. 2015, *ApJ*, **811**, 40
 Sun, X. H., Reich, W., Waelkens, A., & Enßlin, T. A. 2008, *A&A*, **477**, 573
 Taylor, A. R., Stil, J. M., & Sunstrum, C. 2009, *ApJ*, **702**, 1230
 Testori, J. C., Reich, P., & Reich, W. 2008, *A&A*, **484**, 733
 Thomson, A. J. M., Landecker, T. L., Dickey, J. M., et al. 2019, *MNRAS*, **487**, 4751
 Urošević, D., Arbutina, B., & Onić, D. 2019, *Ap&SS*, **364**, 185
 Van Eck, C. L., Brown, J. C., Ordog, A., et al. 2021, *ApJS*, **253**, 48
 Van Eck, C. L., Brown, J. C., Stil, J. M., et al. 2011, *ApJ*, **728**, 97
 Wendell, H. J., Higgs, L. A., & Landecker, T. L. 1991, *A&A*, **241**, 551
 Wolleben, M., Fletcher, A., Landecker, T. L., et al. 2010a, *ApJL*, **724**, L48
 Wolleben, M., Landecker, T. L., Carretti, E., et al. 2009, in *IAU Symp. 259, Cosmic Magnetic Fields: From Planets, to Stars and Galaxies*, ed. K. G. Strassmeier, A. G. Kosovichev, & J. E. Beckman (Cambridge: Cambridge Univ. Press), 89
 Wolleben, M., Landecker, T. L., Carretti, E., et al. 2019, *AJ*, **158**, 44
 Wolleben, M., Landecker, T. L., Hovey, G. J., et al. 2010b, *AJ*, **139**, 1681
 Wolleben, M., Landecker, T. L., Reich, W., & Wielebinski, R. 2006, *A&A*, **448**, A11
 Xu, W. F., Gao, X. Y., Han, J. L., & Liu, F. S. 2013, *A&A*, **559**, A81